ENGINYERIA ELECTRÒNICA ELÈCTRICA I AUTOMÀTICA

UNIVERSITAT ROVIRA I VIRGILI

Graduate Students Meeting on Electronics Engineering

Tarragona and Online, June 29th and 30th, 2022

BOOK OF ABSTRACTS

ENGINYERIA ELECTRÒNICA ELÈCTRICA I AUTOMÀTICA
UNIVERSITAT ROVIRA I VIRGILI
Graduate Students Meeting on Electronics Engineering
Tarragona and Online, July 1st and 2nd, 2021

Program

Wednesday, July 29th

14.20 - Opening

14.30 – Invited: Enrique Miranda (Universitat Autònoma de Barcelona, Spain)

“Compact modeling of memristive devices for neuromorphic computing”

15.30 – Invited: Samar Saha (Prospicient Devices, USA)

“Physical Principles to Formulate Thin Film Transistor Models for Circuit Design”

17.00 – Ph. D. Student Oral Presentations:

Beatriu Domingo - “Transient absorption spectroscopy study of an iron porphyrin–TiO2 hybrid system for CO2 reduction”

Anand Ambily - “Development of a novel carbonized porous silicon electrochemical sensing platform by pyrolysis of furfuryl alcohol”

Marc Lázaro - “Custom backscatter modulation based on CSS signals with an enhanced processing gain”

Thursday, June 30th

9.20 - Opening

9.30 – Invited: Luis Fernando da Silva (Federal University of Sao Carlos, Brasil)

“Functional Materials: Processing and Characterization”

10.30 – Coffee Break and Poster Session

11.00 – Ph. D. Students Oral Presentations

- Lluc Sementé - “Cleaning Mass Spectrometry Imaging data using a matrix perspective”

- Christian Roemer - “Modeling Approach for Injection and Channel-Resistance Effects in Schottky Barrier Field-Effect Transistors”

- Deepanshu Verma - “Porous alumina based bio-sensing platform for early-stage infection diagnosis”

- Ramon Estalella - “Numerical Methods for the Robust Stability and Performance of Power Conversion Systems”

12:00 – Invited: Małgorzata Norek (Military University of Technology, Poland)

“Porous anodic alumina (PAA) and synthesis of functional nanomaterials based on PAA”

13.00 – Closing and Lunch

Keynote Talks

Małgorzata Norek

Porous anodic alumina (PAA) and synthesis of functional nanomaterials based on PAA

Porous anodic alumina (PAA) is fabricated by electrochemical oxidation of aluminum. Self-organized growth of PAA resulting in a hexagonal close-packed (hcp) structure of pores occurs only within narrow anodization conditions. Usually these conditions are limited to a given voltage dependent on the acid species. Pore arrangement is also influenced by state of Al substrate. Pore shape can be easily modulated by external electrochemical parameters such as applied voltage or current. This correlation is a base for designing various 1-dimensional photonic crystals (PCs). In the PCs, the effective refractive index is controlled by periodically modulated porosity along the whole PAA thickness. By application of well-designed pulse modalities and electrochemical conditions the gradient-index and step-index optical filters with photonic stop bands ranging from visible to mid-infrared spectral range can be produced. Moreover, PAA can be used for templated synthesis of other functional nanomaterials, such as ZnO.

Luis Fernando da Silva

Functional Materials: Processing and Characterization

Functional materials are materials that exhibit practical applications in various areas, such as Physics, Chemistry, Engineering, Biology, among others. Some examples of applications are the light-emitting-diodes “LEDs”, catalysts, (bios)sensors, Li-ion batteries, and organic solar cells. This class of materials contributed to the development of the current society, contributing to improve our health, safety, and wellness. Despite the promising aspects of functional materials, researchers have devoted attention to enhancing the performance of traditional materials, or even to engineer novel functional materials. However, to obtain promising materials is essential a careful preparation as well as characterization of the properties of these materials to guarantee the reproducibility of their performance aiming for industrial purposes. In this presentation, it will be presented some methodologies applied to obtain micro and nanosized functional materials, and the importance of processing parameters. Also, we will talk about the importance of conventional and advanced characterization techniques applied in materials characterization.

ENGINYERIA ELECTRÒNICA ELÈCTRICA I AUTOMÀTICA

UNIVERSITAT ROVIRA I VIRGILI

Graduate Students Meeting on Electronics Engineering

Students Proceedings

Synthesis conditions optimization and NO_2 gas sensing response of zinc oxide (ZnO) hierarchical nanostructures

Shuja Bashir Malik, Eduard Llobet Valero

MINOS, DEEEA, Universitat Rovira i Virgili, Països Catalans 26, 43007 Tarragona, Spain
shujabashir.malik@urv.cat, eduard.llobet@urv.cat

Abstract

ZnO nanostructures with floral morphologies were synthesized using hydrothermal synthesis at 150 ºC. The powdered samples were characterized for structural and morphological properties by X-ray diffraction (XRD) and Field Emission Scanning Electron Microscopy (FESEM) respectively. XRD studies confirmed the formation of hexagonal wurtzite structure of ZnO. The average crystallite size of the prepared nanopillars and nanoflowers were found to be 25 nm and 24 nm respectively. FESEM confirmed the formation of two structures. Assemblies of 2 - 3.5 µm nanopillars are formed at longer reaction time while as floral structures (~4 µm) with petals are formed at short reaction time. The ZnO nanostructures show excellent sensing response towards 1ppm NO_2. The sensors fabricated with the ZnO nanostructures show the best sensing response at 150 ºC. The highest response (R_{gas}/R_{air}) recorded in case of ZnO nanoflowers (NF) was 50 and in case of ZnO nanopillars (NP) was 40. The response of nanoflowers is higher which is attributed to its higher surface area and higher surface defects.

Keywords: Hydrothermal synthesis, gas sensing, hierarchical nanostructures

1. Introduction

Rampant use of fossil fuels for automobiles, electricity generation and industries lead to tremendous emission of greenhouse gases which are responsible for global warming [1]. Emission of hazardous gases by burning fossil fuel has led to a drastic increase in air pollution. The pollutants are toxic gases and volatile organic compounds (VOCs) which lead to major health problems [2]. Development of sensors for detection and monitoring of these pollutants is a highly critical area of research. Owing to their low cost, high stability, small size, and the suitability to detect both reducing and oxidizing gases [2], metal oxide semiconductor (MOS) gas sensors are being widely used. Among all the MOS, zinc oxide (ZnO) is highly desirable for its unique properties like non-toxicity, good optical properties, stability, and wide band gap (3.37 eV) at room temperature [3]. Keeping in view these distinctive properties of ZnO, it was chosen as a candidate for gas sensing applications.

In this work, we report the synthesis of ZnO hierarchical nanostructure growth by facile hydrothermal method at low temperature (150 ºC). Nanoflowers were synthesized at short reaction times while as nano pillar assemblies were synthesized at higher reaction times. It was observed that the growth of the nanostructures is dependent on various factors like precursor concentration, reaction temperature, reaction time and pH. Several synthesis reactions were checked to examine the reproducibility of the reaction method and to optimize the synthesis conditions of the desired nanostructures. Gas sensing properties of synthesized ZnO nanostructures were analyzed by exposing the nanostructures to 1ppm NO_2. The results reveal the dependance of sensing properties on the morphology of the nanostructures and operating temperature.

2. Results

The crystal structure of the as-synthesized ZnO nanostructures was analysed by XRD. The diffraction patterns (Figure 1) are indexed to hexagonal wurtzite ZnO phase JCPDS card no. 01-075-1526. The crystal structure matches the space group of P63mc with lattice constant a= 0.3241 nm and c= 0.5195 nm for nanopillars and a= 0.3239 nm and c= 0.5188 nm for nano flowers. No characteristic peaks from other phases or impurities were observed indicating high purity of the prepared samples. Also, the strong and sharp peaks indicate high crystallinity of the prepared samples. The average crystallite sizes of nano pillars and nano flowers calculated by Scherer's formula are 25 nm and 24 nm respectively. Figure 2 shows FESEM images of as prepared ZnO nano pillars (top) and ZnO nanoflowers (bottom). Nanoflowers with an average size of ~ 4 µm were synthesized at lower reaction times while as nano pillar assemblies with an average size of ~ 3.5 µm were obtained at higher reaction times. The pillar assemblies are clusters of more than a dozen tapered hexagonal prism like ZnO nanorods with an average size of ~900 nm. As can be seen from the FESEM images (Figure 2, bottom), the nanoflowers have many hollow structures and pores. The petals of the nanoflowers are rough which can be attributed to the clustering of the nanosized ZnO particles.

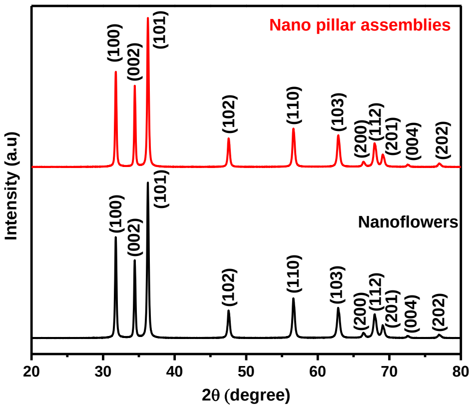

Figure 1: XRD patterns of as-prepared ZnO nanopillar assemblies and ZnO nanoflowers.

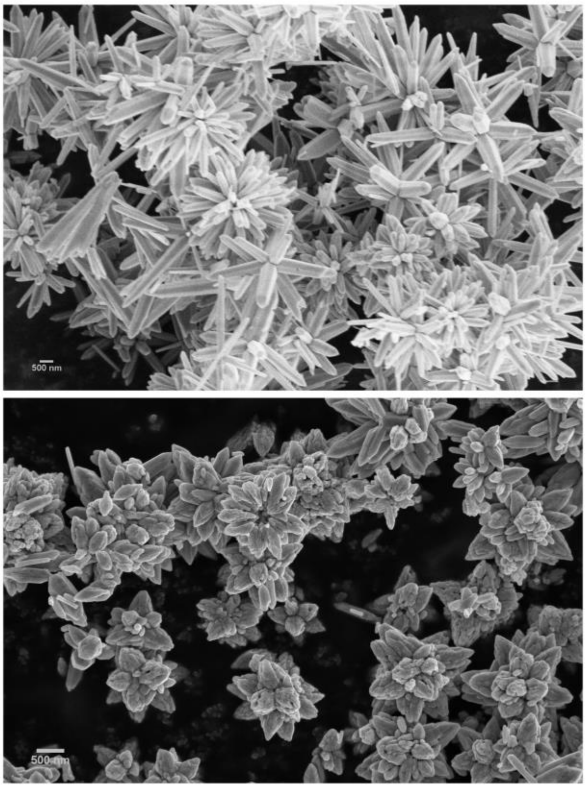

Figure 2: FESEM image of as prepared ZnO nano pillars (top) and ZnO nanoflowers (bottom)

The sensors were fabricated onto commercial alumina substrates by drop coating technique. A specific amount of the ZnO nanostructures was suspended in 1,2-propanediol and sonicated in an Eppendorf. The solution was dropped onto the electrodes of the alumina substrate employing a micropipette. The resulting film was annealed at 500 ºC for 2 hours in a muffle furnace in synthetic air. The gas sensing results were studied by exposing the ZnO films to 1ppm of NO_2 gas for 10 minutes. For gas sensing measurements the sensors were kept in an airtight Teflon chamber. Before exposing the sensors to NO_2, the sensors were stabilized under dry air flow for 2 hours.

The sensing responses of the sensors were studied at 150 ºC, 200 ºC and 250 ºC. The sensors showed highest response towards NO_2 at 150 ºC. The highest responses registered at different temperatures are shown in Figure 3.

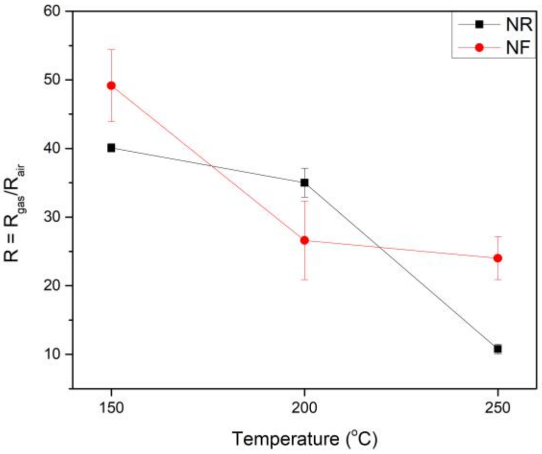

Figure 3: Highest sensor responses at different temperatures towards 1ppm NO_2.

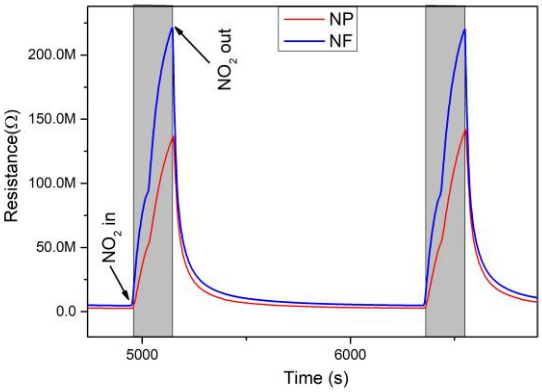

Figure 4: Typical response behaviour of ZnO nanostructures towards 1ppm NO_2 at 150 ºC

The typical behaviour of an n-type semiconductor (ZnO) exposed to repeated response and recovery cycles of NO_2 - an oxidizing gas is shown in Figure 4. When an n-type metal oxide is exposed to atmospheric oxygen, depending on the temperature the oxygen gets adsorbed onto the surface of the metal oxide in different molecular and atomic states. It has been found that when the operating temperature is between 100 and 150 ^oC, the dominating oxygen species are O_2^-, when the working temperature is raised from 150 to 200 ^oC the dominant oxygen species are atomic oxygen (O^-) and further increase in the temperature leads to the formation of O^{2-} [4]. The molecules of the oxidizing gas reaching the surface of ZnO get adsorbed on the surface acting as surface-acceptors immobilizing conduction electrons thus increasing the resistance of the material (ZnO). During the cleaning cycle, the adsorbed species are removed from the surface recovering the previous resistance values [3]. Higher responses towards NO_2 by ZnO nanoflowers over nano pillars may be attributed to the higher surface area of the floral morphologies [5].

3. Conclusions

Desired hierarchical ZnO nanostructures were successfully synthesized with great reproducibility using a facile one-pot hydrothermal synthesis. An excellent sensitivity is shown by the ZnO nanostructures towards 1ppm NO_2 with the highest response recorded at 150 ^oC.

4. Acknowledgements

This project has received funding under Martí-Franquès Research grants Programme, Doctoral grants – 2019, (2019PMF-PIPF-14).

References

[1] S. Sitch, V. Brovkin, W. von Bloh, D. van Vuuren, B. Eickhout, and A. Ganopolski, “Impacts of future land cover changes on atmospheric CO2 and climate,” *Global Biogeochem. Cycles*, vol. 19, no. 2, pp. 1–15, 2005, doi: 10.1029/2004GB002311.

[2] M. J. S. Spencer, “Gas sensing applications of 1D-nanostructured zinc oxide: Insights from density functional theory calculations,” *Prog. Mater. Sci.*, vol. 57, no. 3, pp. 437–486, 2012, doi: 10.1016/j.pmatsci.2011.06.001.

[3] S. Agarwal, P. Rai, E. Navarrete, E. Llobet, and F. Güell, “Sensors and Actuators B : Chemical Gas sensing properties of ZnO nanostructures (fl owers / rods) synthesized by hydrothermal method,” vol. 292, no. February, pp. 24–31, 2019.

[4] N. Barsan and U. Weimar, “Conduction model of metal oxide gas sensors,” *J. Electroceramics*, vol. 7, no. 3, pp. 143–167, 2001, doi: 10.1023/A:1014405811371.

[5] Z. Yuan, X. Jiaqiang, X. Qun, L. Hui, P. Qingyi, and X. Pengcheng, “Brush-like hierarchical zno nanostructures: synthesis, photoluminescence and gas sensor properties,” *J. Phys. Chem. C*, vol. 113, no. 9, pp. 3430–3435, 2009, doi: 10.1021/jp8092258.

Physics Based Compact Model for 2DFETs

A. Mounir[1], B. Iñiguez[1], F. Lime[1], T. Knobloch[2], T. Grasser[2]

[1] Rovira I Virgili University, Tarragona, Spain. (ahmed.mounir@urv.cat)
[2]Institute for Microelectronics (TU Wien), Vienna, Austria

Abstract

A physics based analytical DC compact model for single-gated (back-gated) MoS$_2$ FET is presented. The model is developed by calculating the charge inside the 2D layer using a few reasonable approximations and is expressed in terms of the Lambert W function. The current is then calculated in terms of the charge densities at the drain and source. We report a new observation for the transfer characteristics, where a super linear conduction for the current is observed above certain gate voltages. This effect is correctly modelled by means of an effective mobility expression. Despite the relative simplicity of the model, it shows very good agreement with the experimental data measured on monolayer MoS$_2$ transistors with a channel length of 2 µm, a channel width of 10 µm, and 25 nm SiO$_2$ as a gate oxide. The monolayer MoS$_2$ channel was grown by CVD at 850 °C directly on SiO$_2$(25nm)/p++-Si substrates.

1. Introduction

The use of 2D materials as the conducting channel in Field Effect Transistors (FETs) has been under research as an alternative rather than Si. The thin thickness for 2D materials provides the ultimate scalability in FETs, which translates to a higher gate electrostatic controllability over the channel and compared to 3D gate structures it has less parasitic. To use those new devices in VLSI circuits, compact models needed to be developed, which are sets of equations describing the I-V and C-V characteristics of the device. In this paper, we have developed a unified charge compact model describing the DC characteristics for a MoS2 FET. Our model is based on [1] and is validated against different technologies with single/double gate structures. For the sake of the limited page number, we present here only the validation with single (back) gate FET.

2. Model Development

In developing our physics based compact model, we start by modeling the electrostatics of the device. Our work is based on [1], in which the electrostatics can be written as following adopting it to the single gate structure,

$$Q_{net}(x)\ +Q_{it}(x)\ =-C_b\big(V_b-V_{\mathrm{b0}}-V(x)+V_c(x)\big) \quad (1)$$

Where $Q_{net}(x)$ is the total mobile charge density, $Q_{it}(x)$ is the interface trap charge density, C_b is the bottom oxide capacitance per unit area $C=\frac{\varepsilon_0\varepsilon_b}{t_b}$ and $(V_b-V_{\mathrm{b0}}\ )$ is the back overdrive gate voltage, where V_{b0} takes into account the work function difference and any possible additional charges due to impurities or doping. The interface trap charge density $Q_{it}(x)$ is significant in MoS2 FET devices. However, we ignore the dependence of $Q_{it}(x)$ on the gate voltage as a first approximation. We consider $Q_{it}(x)$ as a constant value that affects the threshold voltage (VTH) and the subthreshold slop (SS). Thus, V_{b0} is taking account for the interface trap charge. $V(x)$ is the quasi-fermi level along the channel, where $V(x=0)=V_S$ (source voltage) and $V(x=L)=V_D$ (drain voltage). $V_c(x)$ is the shift of the quasi-fermi level with respect to the conduction band.

Another equation for the overall charge density can be expressed as following,

$$Q_{net}(x)\ =-q\,n(x)=\ -C_{dq}V_{th}\ln(1+e^{-\frac{V_c}{V_{th}}}) \quad (2)$$

Where $C_{dq}=q^2D_0$ is defined as the degenerated-quantum capacitance and

$$D_0=\ g_k\left(\frac{m^k}{2\pi hbar^2}\right)+g_Q\left(\frac{m^Q}{2\pi hbar^2}\right)\exp\left(-\frac{\Delta\, E_2}{K_BT}\right) \quad (3)$$

Where D_0 is the 2D density of states. Rearranging equation (2), we get

$$V_c(x)=-V_{th}\ln\left(exp\left(-\frac{Q_{net}}{C_{dq}V_{th}}\right)-1\right) \quad (4)$$

Substituting (3) in (1), we get the uniform charge control model (UCCM) that is expressed as follows,

$$\begin{aligned}Q_{net}(x)-C_bV_{th}\ln\left(exp\left(-\frac{Q_{net}(x)}{C_{dq}V_{th}}\right)-1\right)\\ =-C_b\big(V_b-V_{b0}-V(x)\big)\end{aligned} \quad (5)$$

Equation (5) can be solved numerically to find the total mobile charge density. Numerical solution is not good from compact modeling perspective. Thus, we make an approximation to the polylogarithmic term

$\ln\left(exp\left(-\frac{Q_{net}(x)}{C_{dq}V_{th}}\right)-1\right)$ to develop our core model.

Using Taylor's expansion for the exponential term and some mathematical approximation, we can write the UCCM as follows,

$$Q_{net}(x)-2C_bV_{th}\ln\left(\left(-\frac{Q_{net}(x)}{\sqrt{2}C_{dq}V_{th}}-\frac{\sqrt{2}}{2}\right)\right) = -C_b\left(V_b-V_{b0}-V(x)\right) \tag{6}$$

Equation (6) can be solved to find the total mobile charge inside the semiconductor. To do that, we write (6) in the form of Lambert W function as follows,

$$\left(-\frac{Q_{net}(x)}{2C_bV_{th}}-\frac{C_{dq}}{2C_b}\right)*\exp\left(-\frac{Q_{net}(x)}{2C_bV_{th}}-\frac{C_{dq}}{2C_b}\right) = \frac{\sqrt{2}C_{dq}}{2C_b}\exp\left(-\frac{C_{dq}}{2C_b}\right)\exp\left(\frac{\left(V_b-V_{b0}-V(x)\right)}{2V_{th}}\right) \tag{7}$$

Therefore, the total mobile charge inside the semiconductor can be written as,

$$Q_{net}(x) \approx -2C_bV_{th}\left\{\mathrm{W}\left[\frac{\sqrt{2}C_{dq}}{2C_b}\exp\left(\frac{\left(V_b-V_{b0}-V(x)\right)}{2V_{th}}\right)\right]\right\} \tag{8}$$

Now we have the charge equation expressed in an explicit form using the first branch of Lambert W function. We introduce α and $\beta \approx \frac{\alpha}{2}$ as fitting parameters for the charge equation.

$$Q_{net}(x) \approx -2\beta C_bV_{th}\left\{\mathrm{W}\left[\frac{\sqrt{2}C_{dq}}{2C_b}\exp\left(\frac{\left(V_b-V_{b0}-V(x)\right)}{2\alpha V_{th}}\right)\right]\right\} \tag{9}$$

To calculate the current, we need to calculate the charge equation at the source and drain ends. The current equation can be expressed as,

$$I_{DS}=\frac{W\mu}{L}\left[\frac{Q_D^2-Q_S^2}{2C_b}-V_{th}(Q_D-Q_S) + 2C_{dq}V_{th}^2\ln\left(\frac{Q_D-C_{dq}V_{th}}{Q_S-C_{dq}V_{th}}\right)\right] \tag{10}$$

3. Results and Discussion

Our model is validated against measurement data for three different devices [2]. The devices are fabricated with different gate lengths with a monolayer MoS2 grown by CVD at 850 °C directly on SiO2(25nm)/p++-Si substrates as shown in the following figure.

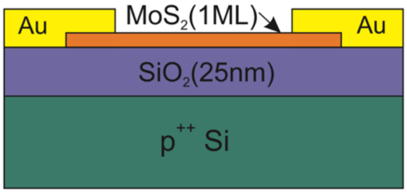

Fig.1 2D schematic for MoS$_2$ FET

After plotting the transfer characteristics of our model against the experimental data, we observe a super linear conduction after certain gate voltage as shown in figure 2. This is to be the first time, as far as our knowledge, to report a super linear conduction for monolayer MoS2 FET for large gate lengths.

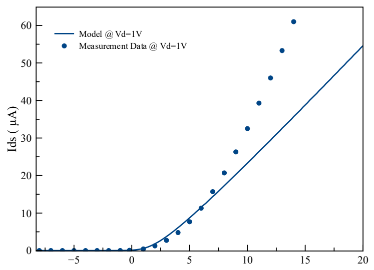

Fig.2 Transfer characteristics at Vd = 1V

To make account for the super linear behavior, we have introduced an empirical term to the current equation. We have different hypothesis for this current increase; however, we need to make more simulation to come to a concrete understanding for this increase. The one introduced here in our model assumes that the mobility increases by increasing the gate voltage. Another assumption for this increase in current might be due to transport due through trap defects.

$$I_{DS}=\frac{W\mu}{L}\,M\left(\frac{V_b}{V_A}+\eta\right)^{\gamma}\left[\frac{Q_D^2-Q_S^2}{2C_b}-2V_{th}(Q_D-Q_S) + 2C_{dq}V_{th}^2\ln\left(\frac{Q_D+C_{dq}V_{th}}{Q_S+C_{dq}V_{th}}\right)\right] \tag{11}$$

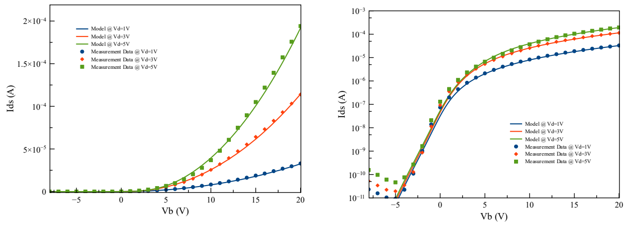

Fig.2 Transfer characteristics for MoS$_2$ FET

7. Conclusions

A physics based analytical DC compact model was developed for single-gated (back-gated) MoS$_2$ FET and shows very good agreement when validating it with experimental data.

References

The references

[1] F. Pasadas et al., “Large-signal model of 2DFETs: compact modeling of terminal charges and intrinsic capacitances,” npj 2D Materials and Applications, vol. 3, no. 1, 2019, doi: 10.1038/s41699-019-0130-6.

[2] Y. Y. Illarionov *et al.*, “Anomalous Instabilities in CVD-MoS2 FETs Suppressed by High-Quality Al2O3 Encapsulation.”

Modeling Approach for Injection and Channel-Resistance Effects in Schottky Barrier Field-Effect Transistors

Christian Roemer, Ghader Darbandy, Mike Schwarz, Benjamín Iñíguez and Alexander Kloes

***Abstract*—In previous iterations of our closed-form and physics-based DC compact model for Schottky barrier field-effect transistors the focus was on the current calculation given by a charge carrier injection over the device's Schottky barriers. With increasing channel lengths of those devices the resistance of this channel must be also considered for higher currents flowing through the device. This work describes a method in order to combine an injection model for Schottky barriers with a channel resistance model.**

***Index Terms*—SBFET, compact modeling, closed-form, Schottky barrier, channel resistance, thermionic emission, field emission, tunneling current**

I. INTRODUCTION

THE Schottky barrier field-effect transistor (SBFET) is an important type of device by itself and also the base for the reconfigurable field-effect transistor (RFET), where both devices have a metal-semiconductor-metal structure and their basic working principle is the blocking mechanism of the source-channel and drain-channel Schottky barriers [1], [2]. Figure 1 shows a schematic cross-section of an SBFET. In [3] we already introduced a closed-form and physics-based compact model that describes the DC characteristics of SBFETs and RFETs by calculating an injection current over a device's Schottky barriers. This model leads to accurate results, as long as the channel resistance of the devices is negligibly small compared to the resistance of the Schottky barriers. For SBFETs with longer channel lengths and RFETs with a longer gate-to-gate distance, the device's channel must be also considered, in order to obtain a good fitting of the DC model for higher currents. Therefore in [4], we made an addition to the DC model to also cover a resistance caused by a longer device channel. While Sec. II covers the important compact model equations, Sec. III shows some results of the model compared to technology computer aided design (TCAD) simulations. Finally, Sec. IV concludes this work.

II. MODELING APPROACH

The SBFET model consists of three main parts that directly affects the total device current. The first two parts are the injection currents over the device's Schottky barriers, which are the field emission (FE) current, given by charge carriers tunneling through the barrier, and the thermionic emission (TE) current, given by charge carriers overcoming the barrier [3], [4]. The FE current is calculated by an equation that approximates the tunneling equation (for electrons in this case)

$$J_{\mathrm{FE}} = \frac{q\mu_{\mathrm{tn}}N_{\mathrm{C}}}{k_{\mathrm{b}}\vartheta} \cdot \int_{\mathcal{E}_{\mathrm{min}}}^{\mathcal{E}_0} f_{\mathrm{m}}(\mathcal{E})[1-f_{\mathrm{ch}}(\mathcal{E})] \times |\vec{E}(\mathcal{E})| \cdot T(\vec{E},\mathcal{E}) \cdot d\mathcal{E}\,, \tag{1}$$

with a solvable integral given as

$$J_{\mathrm{FE}} \approx \frac{q\mu_{\mathrm{tn}}N_{\mathrm{C}}}{k_{\mathrm{b}}\vartheta} \cdot \int_{\mathcal{E}_{\mathrm{min}}}^{\mathcal{E}_0} \frac{1}{4}\exp(-a(\mathcal{E}-E_{\mathrm{f}})^2) \times b \cdot \exp(-c(\mathcal{E}_0-\mathcal{E})) \cdot d\mathcal{E}\,, \tag{2}$$

where q is the elementary charge, N_{C} is the effective density of states in the conduction band, k_{b} is the Boltzmann constant and ϑ is the temperature. The tunneling mobility μ_{tn} for electrons is an adjustable fitting parameter of the model [3]. f_{m} and f_{ch} are the Fermi distribution functions inside the metal contact and the semiconductor channel, $\vec{E}$ is the electric field and T is the tunneling probability, which are all approximated by either the Gaussian distribution or the exponential function in (2) [3]. Parameters a, b and c are energy independent coefficients, and the energy values E_{f}, $\mathcal{E}_{\mathrm{min}}$ and $\mathcal{E}_0$ are calculated from a 2D potential model, that is described in [3].

The TE current is calculated by

$$J_{\mathrm{TE}} = A^*\vartheta^2 \cdot \exp\left(-\frac{q\Phi_{\mathrm{bar}}}{k_{\mathrm{b}}\vartheta}\right) \cdot \left[1-\exp\left(-\frac{qV_{\mathrm{ds}}}{k_{\mathrm{b}}\vartheta}\right)\right] . \tag{3}$$

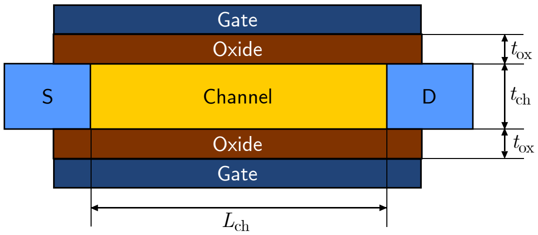

Fig. 1. Schematic cross-section of an SBFET device that is used for the compact model with the relevant geometric parameters.

This project is funded by a grant from TH Mittelhessen University of Applied Sciences, Giessen, Germany. We acknowledge the support by Jens Trommer and Maik Simon from NaMLab gGmbH, Dresden, Germany, André Heinzig from Chair for Nanoelectronics, TU Dresden, Dresden, Germany, Thomas Mikolajick from NaMLab gGmbH, Dresden, Germany and Chair for Nanoelectronics, TU Dresden, Dresden, Germany and Walter M. Weber from Institute of Solid State Electronics, TU Wien, Vienna, Austria.

Christian Roemer is with NanoP, TH Mittelhessen - University of Applied Sciences, Giessen, Germany and DEEEA, Universitat Rovira i Virgili, Tarragona, Spain (e-mail: christian.roemer@ei.thm.de). Ghader Darbandy, Mike Schwarz and Alexander Kloes are with NanoP, TH Mittelhessen - University of Applied Sciences, Giessen, Germany. Benjamín Iñíguez is with DEEEA, Universitat Rovira i Virgili, Tarragona, Spain.

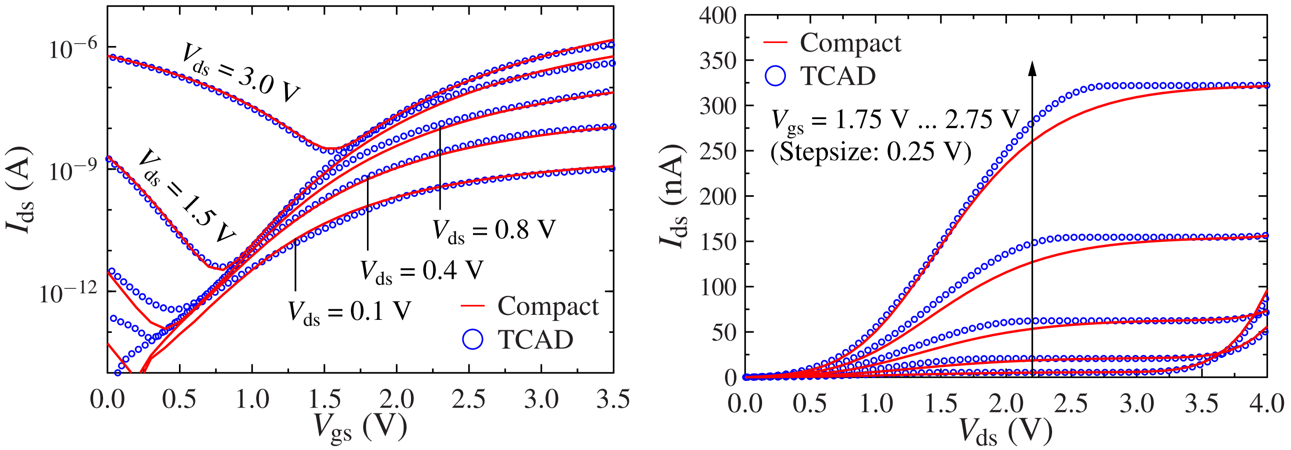

(a)

(b)

Fig. 2. Device characteristics of the SBFET calculated from the compact model (red) and compared to TCAD simulations (blue). The geometries of the simulated device are $L_{\mathrm{ch}} = 5.0\,\mu\mathrm{m}$, radius of the nanowire $= 15\,\mathrm{nm}$ and $t_{\mathrm{ox}} = 6.5\,\mathrm{nm}$ ($\mathrm{SiO_2}$). (a) shows the transfer characteristics for various positive drain voltages in logarithmic scale. (b) shows the output characteristics for various positive gate voltages. The shown characteristics are similar to those form [4].

Here, A^* is the Richardson constant, and Φ_{bar} is the barrier that charge carriers have to overcome [3]. While the TE current is usually only dominant in the device's off-state, the FE current determines the current over the Schottky barrier in the on-state. In order to combine the given equations,

$$I_{\mathrm{inj}} = W_{\mathrm{ch}} \cdot t_{\mathrm{ch}} (J_{\mathrm{FE}} \cdot t_{\mathrm{eff,FE}} + J_{\mathrm{TE}} \cdot t_{\mathrm{eff,TE}}) \tag{4}$$

is used for the total injection current, with t_{ch} as the channel thickness and two effective thicknesses ($t_{\mathrm{eff,FE}}$ and $t_{\mathrm{eff,TE}}$) for each current contribution [3].

The third important part of the device's DC characteristic is the channel resistance, which is calculated as a limiting current by a charge-based metal oxide semiconductor field-effect transistor (MOSFET) equation, given as

$$I_{\mathrm{MOS}} = 2\mu \frac{W}{L} \cdot \left[\frac{k_{\mathrm{b}}\vartheta}{q} \cdot (Q'_{\mathrm{s}} - Q'_{\mathrm{d}}) + \frac{Q'^{2}_{\mathrm{s}} - Q'^{2}_{\mathrm{d}}}{2 \cdot C'_{\mathrm{ox}}} \right], \tag{5}$$

where Q'_{s} and Q'_{d} are the source and drain side charge densities per gate area given by

$$Q'_{\mathrm{s/d}} = \frac{S}{\ln(10)} \cdot C'_{\mathrm{ox}} \cdot W_0 \left(\exp\left(\frac{V_{\mathrm{gs/d}} - V_{\mathrm{T0}}}{S/\ln(10)} \right) \right). \tag{6}$$

Parameter μ is the carrier mobility, W and L are the channel length and width, C'_{ox} is the oxide capacity per gate area and W_0 is the principal branch of the Lambert W function [4]. The parameter S (subthreshold swing) and V_{th} (threshold voltage of the channel MOSFET) are used as fitting parameters [4].

To ensure that the total drain current is limited by either the injection current from (4) or (5), an equation for the total current is introduced as

$$I_{\mathrm{ds}} = \frac{I_{\mathrm{MOS}}}{\sqrt[\gamma_{\mathrm{MOS}}]{1 + \left(\frac{I_{\mathrm{MOS}}}{I_{\mathrm{inj}}}\right)^{\gamma_{\mathrm{MOS}}}}}, \tag{7}$$

which emphasizes the smaller of both currents and has a fitting parameter γ_{MOS} which is used for controlling the transition between the current equations [4].

III. MODEL RESULTS AND VERIFICATION

In order to demonstrate the working principle of the compact model, a TCAD simulation of an SBFET with $L_{\mathrm{ch}} = 5\,\mu\mathrm{m}$ has been performed, using TCAD Sentaurus by Synopsys, Inc. [5]. The results and some additional parameters are shown in Fig. 2, which consist of transfer and output characteristics. Details of the simulation and the model parameters can be found in [4]. As both characteristics demonstrate, the model shows a good agreement to the simulated device, besides a slight deviation in the output characteristics.

IV. CONCLUSION

In this work we demonstrated a straight-forward method in order to combine a Schottky barrier injection model with a channel resistance given by a charged-based MOSFET model, applicable on long channel SBFETs and RFETs with a non-negligible gate-to-gate distance. Additionally, we presented some basic equations of the resulting closed-form and physics-based DC model, as well as some results of the model compared to TCAD simulations, in order to demonstrate its working principle.

REFERENCES

[1] W. Weber, A. Heinzig, J. Trommer, D. Martin, M. Grube, and T. Mikolajick, "Reconfigurable nanowire electronics – a review," *Solid-State Electronics*, vol. 102, pp. 12–24, Dec. 2014.

[2] M. Schwarz, T. Holtij, A. Kloes, and B. Iñíguez, "Compact modeling solutions for short-channel SOI schottky barrier MOSFETs," *Solid-State Electronics*, vol. 82, pp. 86–98, Apr. 2013.

[3] C. Roemer, G. Darbandy, M. Schwarz, J. Trommer, A. Heinzig, T. Mikolajick, W. M. Weber, B. Iniguez, and A. Kloes, "Physics-based DC compact modeling of Schottky barrier and reconfigurable field-effect transistors," *IEEE Journal of the Electron Devices Society*, pp. 1–1, 2021.

[4] C. Roemer, G. Darbandy, M. Schwarz, J. Trommer, M. Simon, A. Heinzig, T. Mikolajick, W. M. Weber, B. Iniguez, and A. Kloes, "Compact modeling of channel-resistance effects in reconfigurable field-effect transistors," in *2022 29th International Conference "Mixed Design of Integrated Circuits and System" (MIXDES)*. IEEE, Jun. 2022.

[5] Synopsys Inc., *TCAD Sentaurus Device User Guide*, 2018, Version O-2018.06.

Transient absorption spectroscopy study of an iron porphyrin–TiO_2 hybrid system for CO_2 reduction

Beatriu Domingo Tafalla[a,*], Tamal Chatterjee[a], Emilio Palomares[a,*,♦,†]

[a]*Institute of Chemical Research of Catalonia (ICIQ), Avinguda del Països Catalans 16, 43007 Tarragona, Spain.*
Tel: +34 977 920 200; E-mail: bdomingo@iciq.es
**Universitat Rovira i Virgili (URV), N5- Edifici de Serveis Centrals Carrer Marcel·lí Domingo, 2-4-6, 43007- Tarragona*
♦*Catalan Institution for Research and Advanced Studies (ICREA), Passeig de Lluis Companys 23, 08010 Barcelona, Spain.*
†*Universidad de Pau y Pays de l'Adour (UPPA), Avenue de l'Université, 64012 Pau, Francia*
Teléfono: +33 5 59 40 70 00.

Molecular catalysts anchored to photocathodes are used as hybrid materials for the (photo)electrocatalytic CO_2 reduction reaction (CO_2RR). The interfacial electron transfer dynamics of such hybrid materials is one of the prime interests for their effective design and functioning. In this work, mesoporous TiO_2-iron porphyrin assembly is used as a model system and Transient absorption spectroscopy (TAS) is employed to investigate the accumulation and lifetime of photogenerated TiO_2 electrons. Upon excitation at 355 nm laser, under applied bias (0—1 V vs. Ag/AgCl) and in the presence of CO_2, our control study showed change in lifetime and decay profile of the photogenerated TiO_2 electrons. This evidences the transference of electrons to the CO_2 from the TiO_2 even in the absence of any molecular catalyst. Finally, in TiO_2 functionalized with iron porphyrins, we observe fast electron recombination features.

Introduction

Generation of useful carbon containing fuels via electro- or photochemical CO_2 reduction (CO_2RR) is a promising lucrative method towards the fossil-fuel independent energy infrastructure in the upcoming decades[1]. In this regard, Earth abundant transition-metal complexes perform CO_2RR with optimal activity and selectivity [2,3] and they offer a good scope to alter their reactivity by tuning their structure[4–6].

For instance, iron porphyrins have been widely explored over more than 30 years[7]. In organic media, they selectively form CO, with high faradaic efficiency in the present of a proton source. With the purpose of boosting its practical application, heterogenization of iron porphyrin certainly broadens the scope of solvent choice, retards the catalyst degradation and facilitates the separation of liquid CO_2RR products.

For the photoelectrochemical CO_2RR, iron porphyrin can be heterogenized on a light absorbing semiconductor material, such as *p*-Si, *p*-GaP, *p*-GaAs, TiO_2, ZnO, NiO, etc.[8] and the assembly can be used as a photocathode[9]. As a solid support, mesoporous TiO_2 offers long-term stability and conductivity under reducing conditions[10], a three-dimensional morphology for high catalyst loading, transparency for spectroelectrochemical characterization of catalytic intermediates and potential to be employed as a photocathode by virtue of its semiconductor nature. Moreover, its activity towards CO_2RR in acetonitrile media has been reported recently[11].

In hybrid photocathode systems, charge accumulation and kinetics of photoinduced electron transfer from the photosensitizer to the molecular catalyst and to the CO_2 are crucial for an efficient CO_2 conversion. In this work, mesoporous anatase TiO_2 is used as a solid photosensitizer support to anchor iron porphyrin-based molecular catalyst. The hybrid system is used as a model system and is characterized by cyclic voltammetry under Ar and CO_2. Furthermore, micro to mili second Transient absorption spectroscopy (TAS) is employed to investigate the accumulation and lifetime of photogenerated electrons in TiO_2 by controlling the applied bias and in the presence of CO_2.

Methods

The iron porphyrin (Fe-Por) was obtained by metalating free base porphyrin (Por) synthesized following a reported method[12].

TiO_2 mesoporous films were prepared by depositing TiO_2 paste (20 nm particle size) on FTO conducting glass substrate by the doctor blade technique[13]. The resulting films were gradually heated up to 500 ºC for sintering. Then, they were functionalized by dip coating into a solution of Fe-Por in MeOH for 30 min at room temperature.

TiO_2 and TiO_2-Fe-Por films where characterized by UV-Vis absorbance spectroscopy and Infra-Red Attenuated total reflectance (IR-ATR).

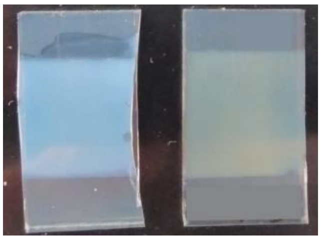

Figure 1. TiO_2 electrode and TiO_2-Fe-Por electrode made by dip coating of TiO_2 in a Fe-Por saturated solution in MeOH for 30 minutes.

Cyclic Voltammetry (CV) measurements of TiO_2, TiO_2-Fe-Por film were carried out in anhydrous $TBAPF_6$/Acetonitrile (0.1 M) electrolyte purged with N_2

or CO_2. Bias was applied using a three-electrode setup[14] with Ag/AgCl (1 M KCl) as the reference electrode and a Pt wire as the counter electrode.

Laser transient absorption spectroscopy (L-TAS) from the microseconds-milliseconds time scale was carried out employing a 355 nm laser as excitation and a lamp used as light probe. All experiments were performed in a Teflon home-made cell with two quartz windows, in $TBAPF_6$/Acetonitrile (0.1 M) electrolyte purged with N_2 or CO_2. Bias was applied using the same three electrode system as for CV

Results and discussion

Fe-Por characteristic Q and Soret bands and -COOH group signals are observed for TiO_2-Fe-Por film by UV-Vis absorbance (Fig. 2A) and IR-ATR spectroscopy (Fig. 1B), respectively, proving the presence of the porphyrin on the TiO_2 film. It is likewise visible at the naked eye on account of the coloration of the film after dip coating into Fe-Por solution (Fig. 1). Cyclic voltammogram of the TiO_2-Fe-Por film in Acetonitrile under argon show the Fe^{II} to Fe^{I} reversible peak. However, such signal is not seen under CO_2 atmosphere, condition in which the TiO_2-Fe-Por behaves mainly as unfunctionalized TiO_2 (Fig. 2C).

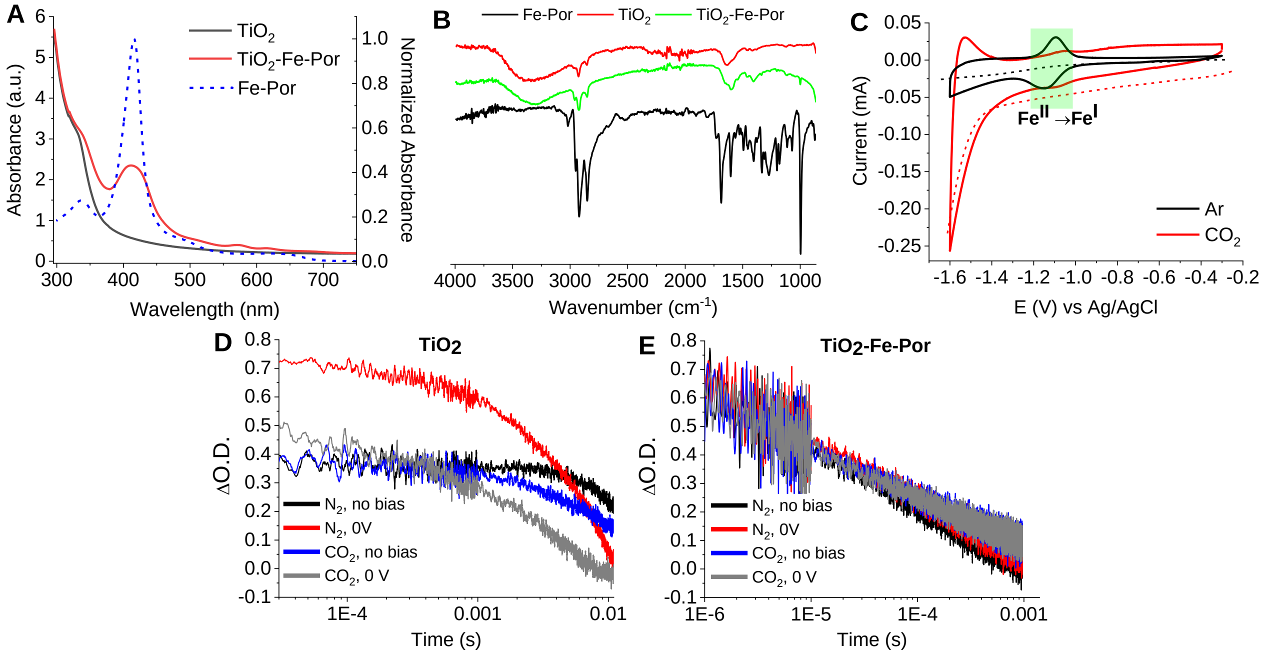

Figure 2. A) UV-Vis absorbance of TiO_2 and TiO_2-Fe-Por films in air and Fe-Por in methanol solution. B) Cyclic voltammograms of TiO_2-Fe-Por film (solid line) and Linear Sweep Voltammograms of TiO_2 film (dashed line) measured in $TBAPF_6$/Acetonitrile (0.1 M) electrolyte at 10 mV/s. C) ATR-IR spectra. D and E) Transient Absorption signals of TiO_2 and TiO_2-Fe-Por films recorded at 680 nm in $TBAPF_6$/Acetonitrile (0.1 M) electrolyte. F) Visual appearance of the TiO_2 and TiO_2-Fe-Por film on FTO glass.

The transient signal of TiO_2 conduction band photogenerated electrons is probed at 680 nm. There is an increase in the transient signal when bias is applied under inert atmosphere, since more electrons populate the TiO_2 valence band and trap states and as a result can be pumped to the excited state in a larger number. Under CO_2, there is a decrease in the transient signal and in the lifetime of the excited electrons (Fig. 2D). This observation stands for a minor and short-lived accumulation of charges in TiO_2 when CO_2 is present, which proves the transference of electrons from the photocathode to the CO_2, even without the molecular catalyst.

For TiO_2-Fe-Por films, the signal of photogenerated TiO_2 electrons decays 100-fold times faster than in unfunctionalized TiO_2, derived from a fast electron transfer from the photocathode to the molecular catalyst. In this case, the transient signal is not affected by the presence of CO_2 or the application of 0 V bias (Fig. 2E).

Table 1. Maximum optical density ($\Delta O.D._{max}$) and time constant ($t_{50\%}$, time to reach half of $\Delta O.D._{max}$) of the excited state of TiO_2 and TiO_2-Fe-Por electrodes.

		TiO_2		TiO_2-Fe-Por	
		$\Delta O.D._{max}$	$t_{50\%}$ (s)	$\Delta O.D._{max}$	$t_{50\%}$ (s)
N_2	no bias	0.13	0.009	0.65	3.6E-5
	0 V	0.73	0.005		
CO_2	no bias	0.3	0.008		
	0 V	0.47	0.001		

As concluding marks, we have been able to functionalize mesoporous TiO_2 films with an iron porphyrin and we have proven the electron transfer from the TiO_2 to the porphyrin. Moreover, to the best of our knowledge, this is the first report evidencing the interfacial electron transfer kinetic of TiO_2 films to the

CO_2. We anticipate that this knowledge will be useful in future while contrasting iron porphyrin-based photocathode assembly for CO_2RR.

Bibliography

1. Son, J., Song, D., Lee, K. R. & Han, J. I. Electrochemical reduction of CO2 on Ag/MnO2 binary catalyst. *J. Environ. Chem. Eng.* **7**, 8–11 (2019).

2. Chen, L. *et al.* Molecular catalysis of the electrochemical and photochemical reduction of CO2 with earth-abundant metal complexes. Selective production of CO vs HCOOH by switching of the metal center. *J. Am. Chem. Soc.* **137**, 10918–10921 (2015).

3. Taheri, A. & Berben, L. A. Tailoring electrocatalysts for selective CO2 or H+ reduction: iron carbonyl clusters as a case study. *Inorg. Chem.* **55**, 378–385 (2016).

4. Hawecker, J., Lehn, J.-M. & Ziessel, R. Electrocatalytic reduction of carbon dioxide mediated by Re (bipy)(CO) 3 Cl (bipy= 2, 2′-bipyridine). *J. Chem. Soc. Chem. Commun.* 328–330 (1984).

5. Kang, P., Chen, Z., Nayak, A., Zhang, S. & Meyer, T. J. Single catalyst electrocatalytic reduction of CO 2 in water to H 2+ CO syngas mixtures with water oxidation to O 2. *Energy Environ. Sci.* **7**, 4007–4012 (2014).

6. Lin, S. *et al.* Covalent organic frameworks comprising cobalt porphyrins for catalytic CO2 reduction in water. *Science (80-.).* **349**, 1208–1213 (2015).

7. Liang, Z., Wang, H.-Y., Zheng, H., Zhang, W. & Cao, R. Porphyrin-based frameworks for oxygen electrocatalysis and catalytic reduction of carbon dioxide. *Chem. Soc. Rev.* **50**, 2540–2581 (2021).

8. Abdinejad, M., Tang, K., Dao, C., Saedy, S. & Burdyny, T. Immobilization strategies for porphyrin-based molecular catalysts for the electroreduction of CO 2. *J. Mater. Chem. A* **10**, 7626–7636 (2022).

9. Garcia Osorio, D. A., Neri, G. & Cowan, A. J. Hybrid photocathodes for carbon dioxide reduction: interfaces for charge separation and selective catalysis. *ChemPhotoChem* **5**, 595–610 (2021).

10. Rosser, T. E., Gross, M. A., Lai, Y.-H. & Reisner, E. Precious-metal free photoelectrochemical water splitting with immobilised molecular Ni and Fe redox catalysts. *Chem. Sci.* **7**, 4024–4035 (2016).

11. Mendieta-Reyes, N. E., Cheuquepán, W., Rodes, A. & Gómez, R. Spectroelectrochemical study of CO2 reduction on TiO2 electrodes in acetonitrile. *ACS Catal.* **10**, 103–113 (2019).

12. Forneli, A. *et al.* The role of para-alkyl substituents on meso-phenyl porphyrin sensitised TiO 2 solar cells: control of the e TiO2/electrolyte+ recombination reaction. *J. Mater. Chem.* **18**, 1652–1658 (2008).

13. Ahmad, M. S., Pandey, A. K. & Abd Rahim, N. Advancements in the development of TiO2 photoanodes and its fabrication methods for dye sensitized solar cell (DSSC) applications. A review. *Renew. Sustain. Energy Rev.* **77**, 89–108 (2017).

14. Chen, S. 2 - Practical Electrochemical Cells. in *Handbook of Electrochemistry* (ed. Zoski, C. G.) 33–56 (Elsevier, 2007). doi:https://doi.org/10.1016/B978-044451958-0.50003-3.

Multi-Omics based machine learning prediction of metabolite levels for knowledge discovery

Trisha Arora [1,2,3], Joaquin Peraire [4,5], Anna Rull [4,5], Núria Canela [2], Xavier Domingo-Almenara [1,2,3]

[1] Computational Metabolomics for Systems Biology Lab, Omics Sciences Unit, Eurecat - Technology Centre of Catalonia, Barcelona, Catalonia, Spain
[2] Centre for Omics Sciences (COS), Eurecat - Technology Centre of Catalonia & Rovira i Virgili University Joint Unit, Unique Scientific and Technical Infrastructures (ICTS), Reus, Catalonia, Spain
[3] Department of Electrical, Electronic and Control Engineering (DEEEA), Universitat Rovira i Virgili, Tarragona, Catalonia, Spain
[4] Hospital Universitari de Tarragona Joan XXIII (IISPV-URV), Tarragona, Spain
[5] Centro de Investigación Biomédica en Red de Enfermedades Infecciosas (CIBERINFEC), Instituto de Salud Carlos III (ISCIII), Madrid, Spain

Abstract

Discovering molecular interactions in biological pathways is of utmost importance in life sciences. Integration of multi-omics data and machine learning paradigms can be used to quantitatively predict changes to reveal associations between different biological layers. Here, machine learning based models quantify the metabolome and identify proteins responsible for variations in metabolite levels, thus enabling the discovery of relationships between proteins and small molecules.

Introduction

Hierarchical and regulatory relationships exist between different layers of biological information. Genomic and epigenomic variations having a direct control on gene expression patterns and the influence of mRNA levels on protein quantities reflect such relationships [1]. Leveraging machine learning to integrate and draw inferences from multi-omics data can provide new insights into different biological conditions [2] that would traditionally not be possible by sampling a single layer of omics data or treating each layer in isolation. Making such predictions could help understand underlying biological mechanisms and reveal unknown connections. Existing reports [2,3] have attempted to predict changes in the metabolome from the proteome using omics profiles from studies with several single gene knockouts. The application of this strategy to multi-omics studies with few phenotypic groups and metabolome prediction from quantitative proteomics with additional information from lipidomics data and vice-versa remains little studied. Therefore, an attempt was made to predict change in metabolites from proteome as well as a combination of proteomics and lipidomics data with few phenotypes. Additionally, feature selection was used to find proteins that are highly correlated to a particular metabolite.

Metabolite prediction using Machine learning

Different machine learning algorithms such as Random Forest, Support Vector Machine (Linear and Radial kernel), XGBoost, Partial Least Squares Regression were used to make the metabolite regression models using proteomics and lipidomics data as features. Multi-omics data from 199 lymphocyte samples was used which contained data from 54 metabolites, 542 proteins and 125 lipids. The models were evaluated on the basis of their 10-fold, 3 repeats cross validation performance. Root mean square error (RMSE), Mean average error (MAE) and the R2 values were used as regression metrics. A comparison was also done when Boruta, which is a random forest-based feature selection method, was used for each metabolite to select important features from the proteome data. Differences in the model performances were also seen using the whole proteome as input features as compared to Boruta selected features being used for metabolite prediction.

Results

Predicting metabolite levels solely from the proteomics data showed cross validation R2 values ranging from 0.065 for aspartic acid to 0.44 for adipic acid (Fig 1), thus showing a large variation in performance depending on the metabolite. Addition of metabolomics data with proteomics as predictor variables lead to an increase in the R2 value for each of the metabolites with 0.95 cross validated R2 for tyrosine. This can be explained by the moderate to strong correlations between different metabolites. However, addition of the lipidomics data showed marginal differences as compared to using proteome and metabolome as predictor variables. Fig. 2 shows better performance when proteomic features selected by the Boruta algorithm were used as input variables than the entire proteome. In this case, the increase in performance also varies depending on the metabolite with a-tocopherol showing almost a 70% increase with selected features.

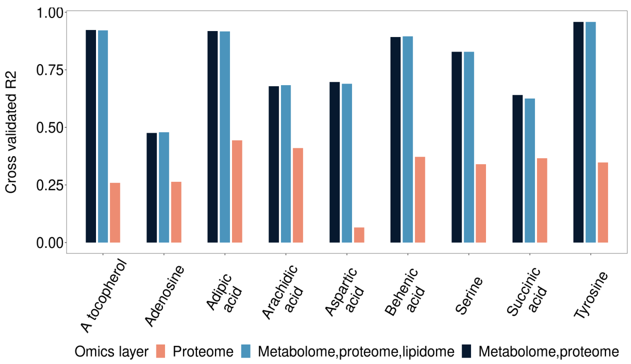

Fig. 1 - Cross validated R2 values for predicting changes in each metabolite from different combination of Omics modalities

Conclusion and Discussion

Performance of prediction models for metabolite concentration from the proteome or combination with metabolome and lipidome depends on the metabolite being predicted. The difference in performance suggests that there exist different levels of regulation that the proteome exerts on the levels of individual metabolites. Interestingly, the addition of lipidomics data to the model did not yield any significant increase in performance despite the known role of lipid species in molecular signaling and their role in mediating different cellular responses. Although intuitive, the prediction models also showed how protein feature selection leads to better performance for predicting metabolite levels rather than the whole proteome. The biological connection between feature selected proteins and metabolites via network analysis and their projection onto biochemical network databases like KEGG or STITCH could reveal new metabolite - protein and even protein - protein interactions.

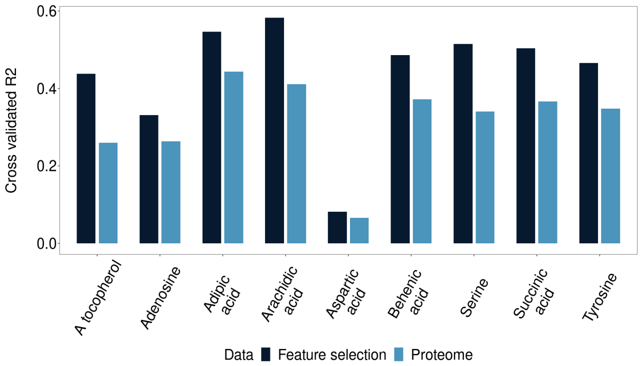

Fig. 2 - Cross validated R2 values for metabolite prediction using the proteome and metabolite specific proteomic features

This approach could eventually lead to better integration of multi - omics data using machine learning paradigms and gain information about molecular interactions that could not be easily inferred by a single omics layer.

References

[1] Z. Cai, R. C. Poulos, J. Liu, and Q. Zhong, "Machine learning for multi-omics data integration in cancer," *iScience*, vol. 25, no. 2, p. 103798, Feb. 2022, doi: 10.1016/j.isci.2022.103798.

[2] Dickinson, Quinn, Aufschnaiter, Andreas, Ott, Martin, and Meyer, Jesse G., "Multi-Omic Integration by Machine Learning (MIMaL) Reveals Protein-Metabolite Connections and New Gene Functions," bioRxiv. [Online]. Available: https://doi.org/10.1101/2022.05.11.491527

[3] A. Zelezniak *et al.*, "Machine Learning Predicts the Yeast Metabolome from the Quantitative Proteome of Kinase Knockouts," *Cell Syst.*, vol. 7, no. 3, pp. 269-283.e6, Sep. 2018, doi: 10.1016/j.cels.2018.08.00

Open-source pre-processing algorithm for GcxGC-MS raw data

Maria Llambrich[1,2], Raquel Cumeras[2,1], Jesús Brezmes[1,2]

[1] Metabolomics Interdisciplinary Group MiL@b, Metabolomics Platform, Department of Electrical Electronic Engineering and Automation, Universitat Rovira i Virgili (URV), IISPV, CERCA, 43007 Tarragona, Spain; phone 977559700; fax 977 55 96 99; maria.llambrich@urv.cat; raquel.cumeras@urv.cat; jesus.brezmes@urv.cat
[2] Biomedical Research Centre, Diabetes and Associated Metabolic Disorders (CIBERDEM), ISCIII, Madrid, Spain

Abstract

Comprehensive gas chromatography is very well suited for the measurement of complex matrices, such those found in metabolomics. However, the high dimensionality of the raw data obtained makes the analysis and processing difficult to use in an automated way. Here we present an open-source workflow for GCxGC data which includes peak detection and identification using public databases. We identified 3 times more peaks compared to the golden standard commercial software. Moreover, 86.6% of the peaks found by the commercial software are present in our workflow too.

1. Introduction

Metabolomics is emerging as a potential tool for diagnosis, characterizing part of the compounds present in a living organism. It is a powerful tool to assess changes in key metabolic pathways which are linked with diseases. The metabolome is formed by small mass compounds present on the human body, particularly on biofluids such as blood, urine, feces or breath. These metabolites are detectable by diverse techniques but the most used are gas-chromatography or liquid-chromatography linked to mass spectrometry (GC/LC-MS). Chromatography allows the separation and characterization of individual compounds in complex samples, whereas mass spectrometry helps in the identification of this compounds [1].

Comprehensive gas chromatography (GCxGC-MS) consists of two columns connected in a serial configuration where a modulator transfers the sample portions on the first column to the second one. Its key advantages are increased peak capacity, increased resolution and increased sensitivity: all highly desirable for simultaneous detection and identification of compounds in complex matrices [2]. Using a non-polar first dimension, analytes are separated according to boiling point and volatility. As the second-dimension separation is fast, it is carried out under essentially isothermal conditions with little influence from sample volatility, so the separation is governed by the specific analyte interactions with the stationary phase. GCxGC-MS data analysis is difficult and time-consuming due to the quantity and complexity of transforming the 3D raw data into chemical information. A typical workflow includes: acquiring data, correct artifacts, detect and identify chemical peaks, and statistical analysis of the datasets [3].

One of the bottlenecks on using this technique is the computer software automation process. Nowadays the huge quantity of data obtained on each measurement are only possible to analyze using commercial software from vendors which are protected and do not allow to automate the entire process. With this purpose, we are developing an automated workflow for an automated complete analysis of GCxGC-MS data in open-source code.

2. Methodology

2.1 Sample analysis

A set of 10 samples from essential oils was analyzed using a 7890 gas chromatogram from Agilent coupled to a Pegasus IV TOF/MS from Leco using a HP5 capillary column (30m × 0.32mm × 0.25mm) and a Rxi-17Si capillary column (1.5m × 0.15mm × 0.15mm). Analyses were performed using headspace into a splitless with helium constant flow of 1 mL·min-1. The GC oven temperature was held at 50°C for 1 min, then raised to 120°C at a rate of 3C/min, then at a rate of 15°C/min until 185°C. The second oven was set at 5°C. The mass spectrometer acquired m/z ratios between 35 and 500Da at 10 Hz and an electron impact energy of 70 eV.

2.2 Data processing

Raw data from the commercial system is transformed to CDF format, which can be imported to the R statistics platform. Chromatographic data requires several pre-processing steps. Based on Cain et al. [4] we had implemented in the workflow the following steps:

i) data centering – mean values are adjusted to 0,

The structure of Comprehensive gas chromatography data is three dimensional. The first dimension is related to retention time from the first column (retention time 1D), retention time for the second column (retention time 2D) is the second dimension and the intensity for each m/z value is the third dimension. In Figure 1 it is shown the total ion chromatogram plot of one of the samples analyzed. Pre-processing steps are applied at each m/z value separately, working with data as two-dimensional corresponding to retention time from first and second column.

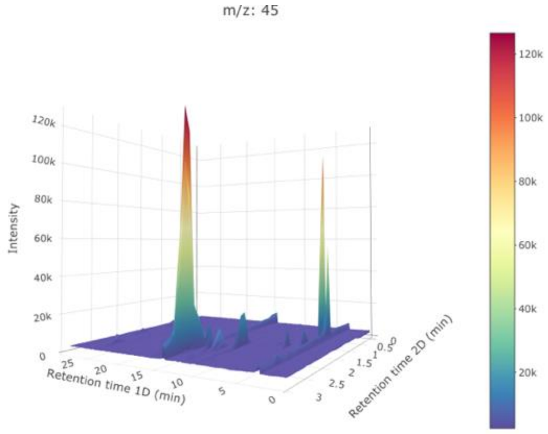

Figure 1. Three-dimensional chromatogram plots of Peppermint essential oil sample analyzed with GCxGC-TOF. Results with the workflow developed showing the results for the m/z 45.

Then automatic peak detection is performed, also known as peak picking. To optimize the procedure we select the regions of interest (ROI) based on the S/N ratio and the watershed algorithm [5] . Deconvolution is applied for ROI regions using Parallel Factor Analysis (PARAFAC) algorithm [6].At last, we obtain a list containing the peak number, retention time 1, retention time 2, intensity and spectra. Identification of the peaks is done comparing the spectra to a reference spectrum from different mass spectrometry libraries using the cosines similarity index [7]. The public libraries used were BinBase (https://binvestigate.fiehnlab.ucdavis.edu/), MONA (https://massbank.us), and GOLM (http://gmd.mpimp-golm.mpg.de).

3. Preliminary results

We have analyzed and processed 10 samples of essential oils, each one having one known essential oil. With our workflow, we have detected an average of 247 (s.d. 41.4) peaks per sample. To validate the method, we checked which of these peaks are detected using the commercial software ChromaTOF from LECO GCxGC-MS instrument. The 88.6% (s.d. 4.6) of peaks detected by the commercial software are detected with our software. In our workflow we are obtaining more peaks compared to the commercial software (see Table 1). There are some steps that are not yet implemented, such as removing duplicated peaks. We used a cut-off for the identification of a similarity index higher than 80%, which was agreed by the 97.6% (s.d. 0.7) of the peaks.

Sample	**Peaks detected using our workflow**	**Peaks detected using commercial software**	**% shared**
Espliego	235	71	84.5
Laurel	250	84	90.3
Lavander	309	92	85.2
Lavandino	241	68	91.9
Coriander	160	47	78.3
Rosemary	287	96	86.5
Peppermint	213	75	90.3
Eucalyptus	218	70	84.3
PetitGrain	200	56	82.3
Caraway	207	68	94.4

Table 1. Results from peak detection on 10 samples using our workflow and a commercial software.

4. Conclusions

Comprehensive gas-chromatography is a promising technique in the metabolomics field. With the workflow we have developed it will be easily implemented in routine analysis. We continue working on the workflow to obtain more accurate results and automatizing all the process.

Acknowledgments

This work has been supported by Spanish MINECO project Total2DChrom [RTI2018-098577-B-C21]. RC is thankful for her EU MSCA-project COLOVOC [798038]. MLL is thankful for her graduate fellowship from URV PMF-PIPF program (ref. 2019PMF-PIPF-37). We acknowledge AGAUR consolidated group grant (2017SGR1119). IISPV is a member of the CERCA Programme/Generalitat de Catalunya.

References

[1] W. Hon Kit Cheung and R. Cumeras, “Basics Of Gas Chromatography Mass Spectrometry System,” in *Volatile organic compound analysis in biomedical diagnosis applications*, Apple Academic Press, 2020, pp. 31–50.

[2] P. Vazquez-Roig and Y. Pico, “Gas chromatography and mass spectroscopy techniques for the detection of chemical contaminants and residues in foods,” in *Chemical Contaminants and Residues in Food*, Elsevier Inc., 2012, pp. 17–61.

[3] S. E. Reichenbach, “Chapter 4 Data Acquisition, Visualization, and Analysis,” *Comprehensive Analytical Chemistry*, vol. 55. Elsevier, pp. 77–106, Jan. 01, 2009, doi: 10.1016/S0166-526X(09)05504-4.

[4] C. N. Cain, S. Schöneich, and R. E. Synovec, “Development of an enhanced total ion current chromatogram algorithm to improve untargeted peak detection,” *Anal. Chem.*, vol. 92, no. 16, pp. 11365–11373, Aug. 2020, doi: 10.1021/acs.analchem.0c02136.

[5] S. Beucher, “Watershed, Hierarchical Segmentation and Waterfall Algorithm,” 1994, pp. 69–76.

[6] J. C. Hoggard, W. C. Siegler, and R. E. Synovec, “Toward automated peak resolution in complete GC × GC-TOFMS chromatograms by PARAFAC,” *J. Chemom.*, vol. 23, no. 7–8, pp. 421–431, Jul. 2009, doi: 10.1002/cem.1239.

[7] K. X. Wan, I. Vidavsky, and M. L. Gross, “Comparing similar spectra: From similarity index to spectral contrast angle,” *J. Am. Soc. Mass Spectrom.*, vol. 13, no. 1, pp. 85–88, 2002, doi: 10.1016/S1044-0305(01)00327-0.

Advanced nanostructures for photonic biosensors

Gohar Ijaz Dar, Lluís F. Marsal
Nanoelectronic and Photonic Systems, Department of Electronics, Electric, and Automatic Control Engineering, Rovira i Virgili University, Avda. Països Catalans 26, 43007 Tarragona, Spain
E-mail: lluis.marsal@urv.cat
E-mail: goharijaz.dar@urv.cat
Phone Number: +34672076677

Abstract

Surface-enhanced Raman spectroscopy (SERS) with enormous enhancements has shown great potential in ultrasensitive detection technologies, but the fabrication of large-scale, controllable, and reproducible substrates with high SERS activity is a major challenge. Here, we report the preparation of Au nanoparticle arrays for SERS-active substrates with tunable particle sizes and interparticle gaps, and the enhancement factor of the SERS signal obtained from 4-mercaptopyridine probe molecules was as high as. As the fabrication protocol of such a SERS substrate is simple and inexpensive, this substrate may anticipate a wide range of applications in SERS-based sensors.

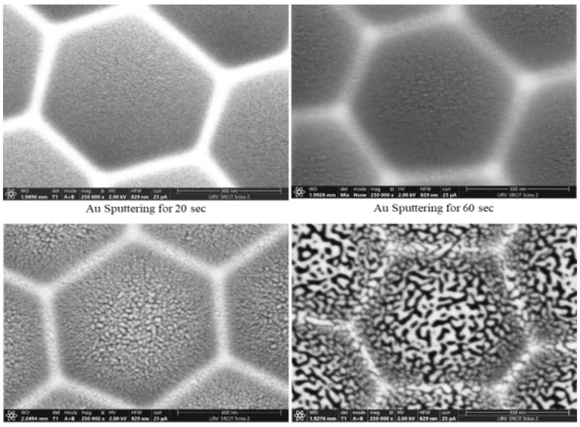

Fig 1. The Al samples with concave-like structures with Au sputtering of 20, 60, 108, and 200 sec.

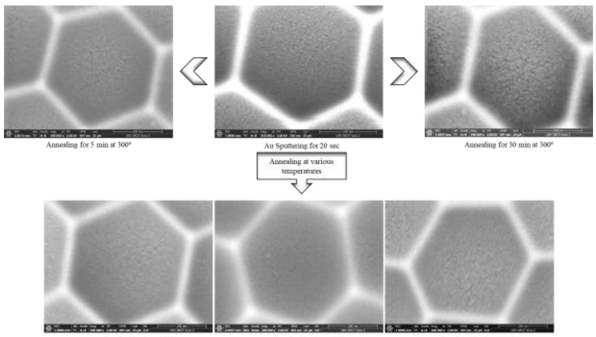
Au Sputtering for 20 sec and annealing at various temperature

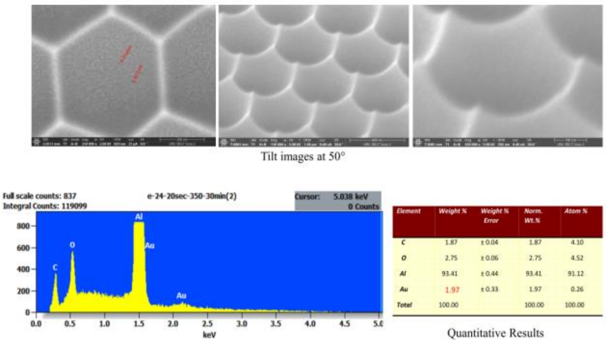
Tilt images at 50°

Element	Weight %	Weight % Error	Norm. Wt.%	Atom %
C	1.87	± 0.04	1.87	4.10
O	2.75	± 0.06	2.75	4.52
Al	93.41	± 0.44	93.41	91.12
Au	1.97	± 0.33	1.97	0.26
Total	100.00		100.00	100.00

Quantitative Results

Fig.2 The FESEM images shown of the prepared Al template with Au sputtering. Au sputtering of 20 sec. Al sheet annealing for various temperatures and times. The Au particle size was measured after annealing (~5 nm). The tilted image of the Al template at 50 degrees showed the concavities. The EDS Spectrum analysis of the template.

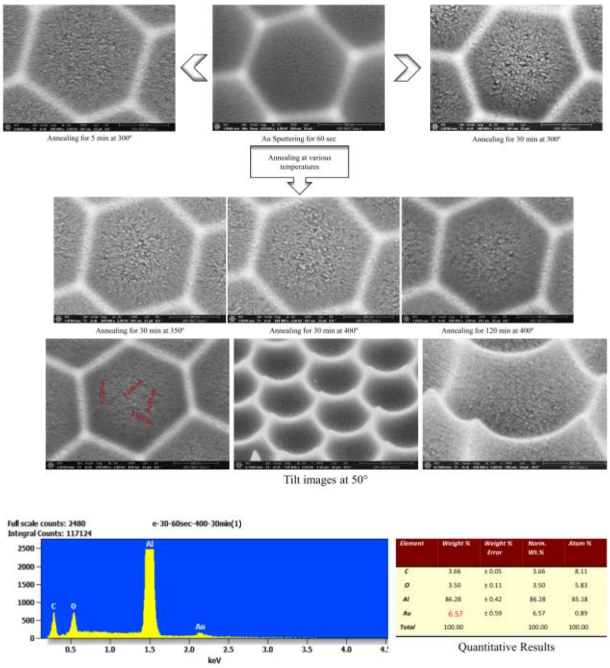
Au Sputtering for 60 sec and annealing at various temperature

Tilt images at 50°

Element	Weight %	Weight % Error	Norm. Wt.%	Atom %
C	3.66	± 0.05	3.66	8.11
O	3.50	± 0.11	3.50	5.83
Al	86.28	± 0.42	86.28	85.18
Au	6.57	± 0.59	6.57	0.89
Total	100.00		100.00	100.00

Quantitative Results

Fig.3 The FESEM images shown of the prepared Al template with Au sputtering. Au sputtering of 60 sec. Al sheet annealing for various temperatures and times The Au particle size was measured after annealing (~8 nm). The tilted image of the Al template at 50 degrees and the EDS Spectrum analysis.

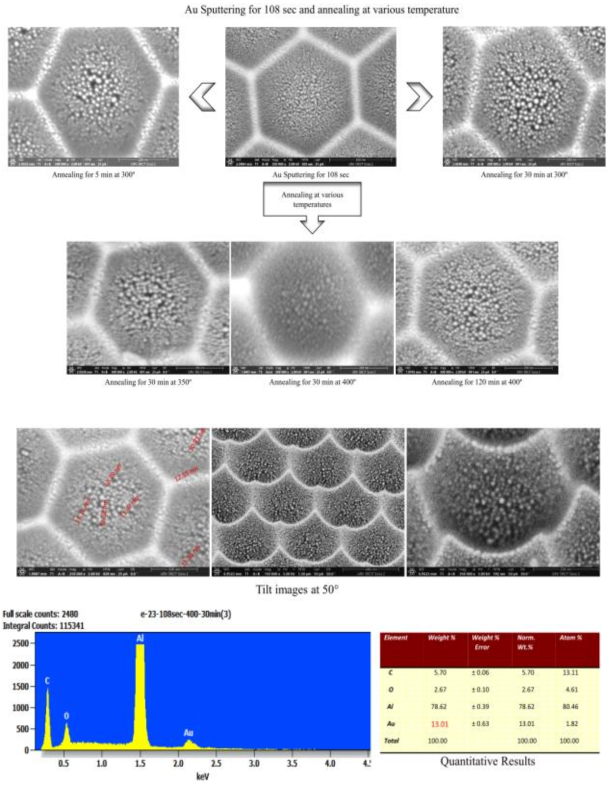

Element	Weight %	Weight % Error	Norm. Wt.%	Atom %
C	5.70	± 0.06	5.70	13.11
O	2.67	± 0.10	2.67	4.61
Al	78.62	± 0.39	78.62	80.46
Au	13.01	± 0.63	13.01	1.82
Total	100.00		100.00	100.00

Quantitative Results

Fig.4 The FESEM images shown of the prepared Al template with Au sputtering. Au sputtering of 60 sec. Al sheet annealing for various temperatures and times The Au particle size was measured after annealing (~13 nm). The tilted image of the Al template at 50 degrees and the EDS Spectrum analysis.

As the various parameters were carried out to deposit the Au film on the Al template and annealed at different temperatures at various intervals of time. The FESEM images revealed that different sizes of particles make the substrate much more efficient for SERS applications owing to high stability and sensitivity. The different particle sizes were obtained (~5, 8, 13, 45 nm) after annealing of Au film deposition (20, 60, 108, and 200 sec).

A two-step anodization process using 0.3 M oxalic acid as an electrolyte at 15 °C and 40 V, as previously described prepared Nanoporous AAO. The first anodization was performed for 18 h, followed by chemical etching of the obtained pores by treatment in an aqueous mixture of chromic acid (1.8 wt %) and phosphoric acid (6 wt %) for 2 h at 70 ° C. The second anodization was executed for 2 h to obtain nanopores. Subsequently, to achieve the concave-like structures Al samples were immersed in an etching solution for 1 h at 70 ° C. For samples prepared through phosphoric acid, we employed the hard and mild anodization process in the first step of anodization. The first step was started with 175 V for initially 3 h and then with a ramping voltage of 0.01 V/sec and reached up to 195 V for 18 h. While working with phosphoric acid keep in mind that due to high voltage the temperature should be as low as -11 °C. The second step was carried out with the same conditions for 2 h to get the nanopores.

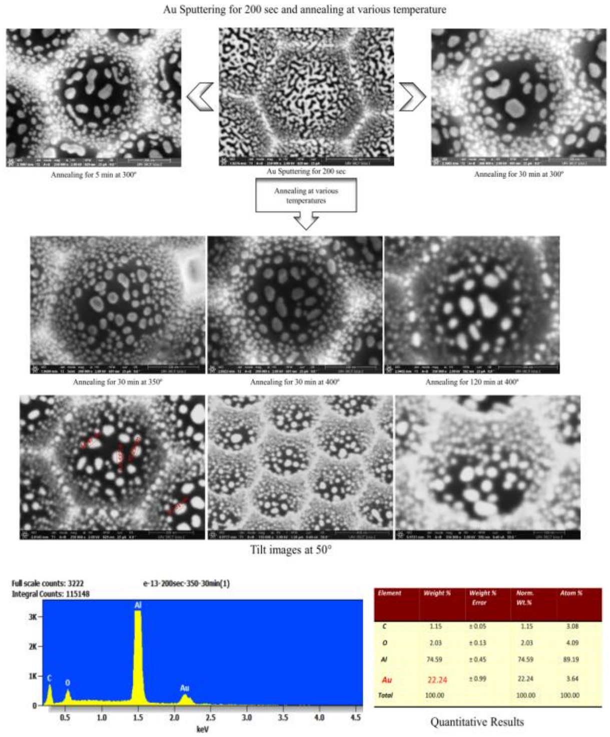

Element	Weight %	Weight % Error	Norm. Wt.%	Atom %
C	1.15	± 0.05	1.15	3.08
O	2.03	± 0.13	2.03	4.09
Al	74.59	± 0.45	74.59	89.19
Au	22.24	± 0.99	22.24	3.64
Total	100.00		100.00	100.00

Quantitative Results

Fig.5 The FESEM images shown of the prepared Al template with Au sputtering. Au sputtering of 60 sec. Al sheet annealing for various temperatures and time The Au particle size measured after annealing (~45 nm). The tilted image of the Al template at 50 degrees and the EDS Spectrum analysis.

Conclusion

In summary, the FESEM analysis showed that the different sputtering conditions and annealing conditions were leads to fascinating structures as SERS substrates for rapid detection of 4- MPY. The combination of these characteristics makes the Al template a highly attractive material for the development of a broad range of sensing devices for many applications. We expect that further progress on structural and chemical modifications of AAO will facilitate the development of AAO-based devices with superior performances. a novel fast SERS strategy will be successfully developed. The assay proved simple, cost-effective, sensitive, and selective for in situ, rapid detection.

References

[1] Choudhari, K. S., et al. "Facile fabrication of superhydrophobic gold loaded nanoporous anodic alumina as surface-enhanced Raman spectroscopy substrates." *Journal of Optics* 24.4 (2022): 044002.

[2] Dong, Jun, et al. "Nanoscale engineering of ring-mounted nanostructure around AAO nanopores for highly sensitive and reliable SERS substrates." *Nanotechnology* 33.13 (2022): 135501.

[3] Toccafondi, Chiara, et al. "Thin nanoporous alumina-based SERS platform for single cell sensing." *Applied Surface Science* 351 (2015): 738-745.

Performance Evaluations of Photonic Crystal-based Biosensor Arrays for Applications to Point-of-Care Diagnostics*

Mubdiul Islam Rizu

Universitat Rovira i Virgili, Phone: +34 671305556, Email: mrizu@ucm.es
*This work has been conducted at: Nanophotonics Research Group, INL, UMR CNRS 5270, INSA-Lyon
7, avenue Jean Capelle, Bâtiment Blaise Pascal, 69621 Villeurbanne Cedex.

Abstract

High-throughput screening is an essential tool for early detection of infectious diseases. With this motivation, the research project CLIPO (Clip-on Optical Biosensor Platform) aims at the development of a cost-effective and handheld optical biochip for reliable as well as multiplexed label-free biosensing in order to fulfil the requirements for point-of-care applications. The biosensing chips consist of arrays of photonic crystal sensors that can be excited at normal incidence yielding high compatibility with simple external reading systems. As a prerequisite for realizing real time biosensing, we have performed all the experiments in various solvent and aqueous media (e.g. water, ethanol/water, and glucose/water) to study the sensor responses and measured the sensitivity of the biochip. After all these experiments, we have come to the conclusion that our photonic crystal sensors show good reproducibility, stability and sensitivity compared to the state-of-the-art.

1. Introduction

There are strong economic interests and societal issues to develop low-cost diagnosis systems, both in developing countries where preventing epidemics at the early stage is crucial, and in developed countries where the cost of healthcare becomes an important issue [1]. The underlying motivation for CLIPO are the new requirements for environmental, food and health monitoring, which lead to a growing need for new types of sensors enabling fast, simple and reliable molecular analysis [2]. Among such devices, optical biochips designed for label-free and multiple parallel sensing are of high interest for many applications such as cost-effective detection of specific illnesses via the evidence of biomarkers in body fluids [3]. The research on photonic biosensors aims at the realization of biochips which are compatible with external reading systems, such as scanners or cameras. The transducers consist of photonic-crystal [4] devices excited at normal incidence and with strongly varying transmission/reflection behavior in presence of target biomolecules [5].

In this context, my work was to deal with optical characterization of the fabricated chips. In particular, the objective of my internship was to validate the performances of the fabricated biochips in terms of reproducibility, reliability and sensitivity by a thorough optical characterization of individual photonic crystal sensors and the study of their responses in various media. More details will be provided later in the experimental methods section.

2. Photonic Crystal Based Sensor

The industrial collaborative research project CLIPO aims at developing and demonstrating a cost-effective and handheld optical system for reliable, multiplexed label-free biosensing, which offers a high potential to greatly overcome the current sensitivity limits of the existing systems. The system contains a clip-on disposable optical chip consisting of an array of nanophotonic biosensors that are read using a lens-free camera as shown in figure 1. The biosensors are separated by highly-insulating optical barriers ensuring high signal-to-noise ratio of the detected signal and low crosstalk between sensors. The clip-on chip is fabricated mature silicon technology, allowing for low costs and mass production.

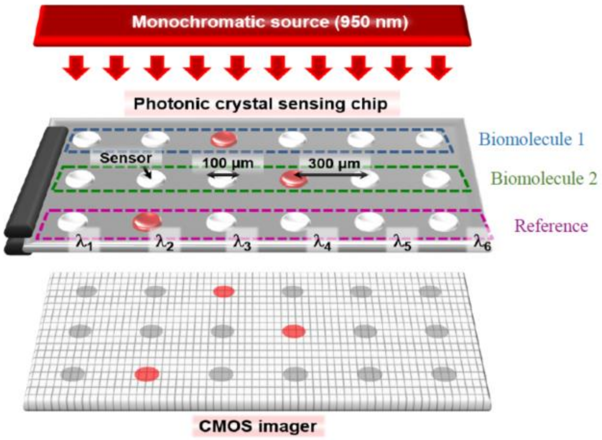

Fig.1. Artistic view of the principle of the CLIPO architecture.

In order to provide efficient and sensitive read-out using this architecture, the optical chip needs to yield good excitation at normal incidence, a measurable resonance shift depending on refractive index variations (i.e., good sensitivity) and the ability to translate this shift into readable data directly on the CMOS camera. As described below, Photonic Crystals (PhCs) enable to fulfil these requirements. In figure 1, each sensor is made of a PhC. The sensor array consists of several identical lines of individual sensors, in order to enable multiplexing (i.e., each line could be detecting a different analyte from the other lines). In each line, the PhCs are all different in order to have only one device resonating at the wavelength of the monochromatic source and detected on the camera. As will be explained later, this enables the direct read-out of any shift of resonance wavelength.

3. Experimental Set-up and Methods

The standard dimension of each PhC sensor is 100 x 100 µm, and the sensor spacing is 300 nm. The exact parameters of each PhC along an “integrated spectrometer” line are different from its neighbors, but the period is around a ~ 300 nm, and each PhC consists of alternating rows with large radius R_1 ~ 100 nm and small radius R_2 ~ 90 nm. The targeted spectral range for a line of PhC is between 920 nm and 970 nm, with a resonance wavelength that is incremented via the design of each photonic crystal. The chip has 32 identical rows made of 32 PhCs with increasing resonance wavelength. Figure 2 shows the photograph of one of the chips, with the 1 cm^2 sensor array in the middle, as well as the chip layout.

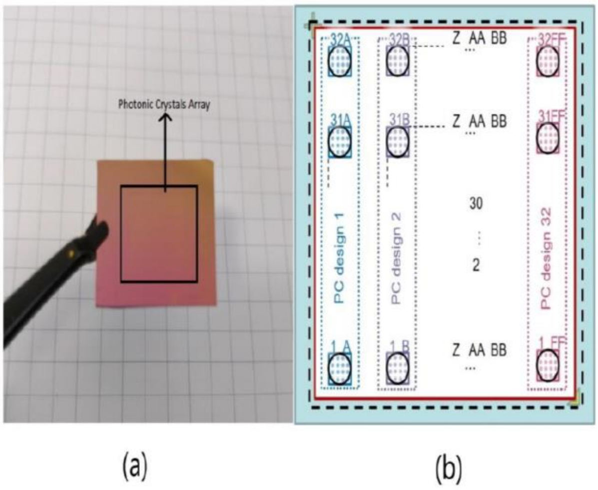

Fig.2. (a) Photograph of one of the sensor chip, (b) artistic view of the chip layout with its array of 32 x 32 PhC sensors.

A complex optical set-up is needed for the individual characterization of the sensors of the chip. The principle of the bench is shown in figure 3. The characterization is done via spectral micro-reflectivity measurements. As a light source, a super LED covering a wide range of wavelengths (750 - 1100 nm) is used for the illumination. The sample is excited by a free space polarized beam going through polarization controller and focused by microscopic objective. A first beam splitter is placed on the optical path in order to separate the incident beam from the beam reflected by the sample. A second beam splitter is then placed on the reflected beam path, in order to send half of the reflected signal to the optical spectrum analyzer while the other half goes towards a near infrared camera via an optical lens. Here, the camera is used as a visualization tool to position the beam on the PhC sensors.

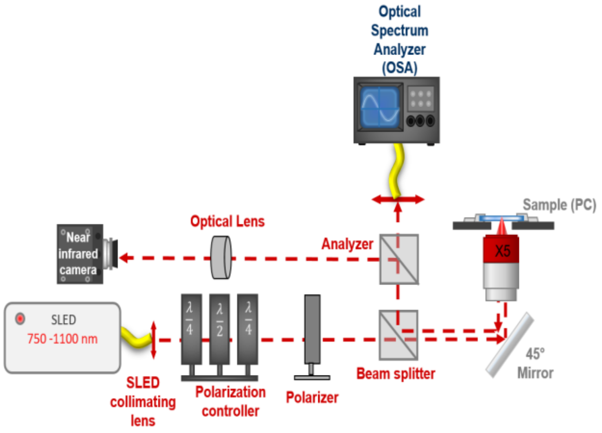

Fig.3. Artistic view of the optical set-up for sensor characterization.

Before performing characterization, the chip needs to be prepared for measurements in liquid medium. This is performed in two steps: first, a surface preparation to get a clean surface with perfect wettability, and secondly, the realization of a pool onto the sample surface to confine the liquid on the PhC array. Both steps are absolutely crucial to obtain a good reproducibility of measurements.

First Step: At first, the sample is cleaned with deionized water with carefully controlled resistivity. Then, it is cleaned with acetone to remove organic impurities. Following that, ethanol is used to remove residual traces of acetone and other impurities. Then an ozone treatment is performed to the chip to make the surface hydrophilic.

Second Step: To study the sensors performance without any risk of alteration of the liquid and/or the conditions, the sample solution (e.g. water, ethanol etc.) needs to be infiltrated in the photonic crystal holes and confined by making a liquid pool over the chip. The pool consists of a polydimethylsiloxane (PDMS) ring placed around the sensing area, as shown in figure 4. After the liquid is infiltrated, the pool is covered by a thin cover glass in order to prevent evaporation as well as impurities deposition, and to obtain a flat top surface, which eliminates distortion effects on the visualization camera. In order to ensure that no alteration of the liquid has occurred during the measurements, the refractive index of the solution is systematically measured before each experiment using a refractometer, and compared to the refractive index of the liquid contained in the pool after the experiment.

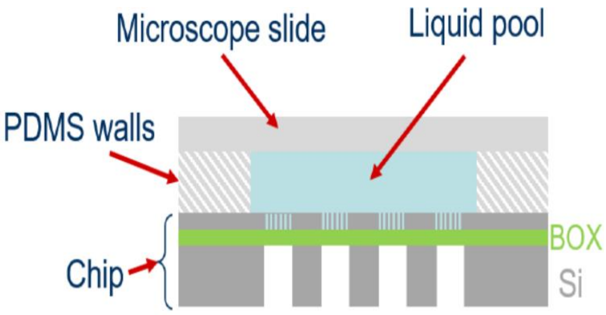

Fig.4. Artistic view of the liquid pool on the photonic chip.

4. Results and Discussions

In this section, the experimental results, statistics and analysis collected from the optical characterization in terms of reproducibility, stability and sensitivity for glucose/water solution will be discussed.

Stability Test: Two different types of sugar/water mixtures have been studied i.e. sucrose/water and glucose/water. As the results obtained for sucrose did not show any good stability, I have focused here on the results for glucose. The concentration of glucose has been arbitrarily chosen to be 100 g/l (1 g of glucose powder mixed in 10 ml deionized water). After preparing the solution, I have measured its refractive index in the refractometer for 2 hours. In figure 5, the stability of refractive index for the glucose/water solution is shown.

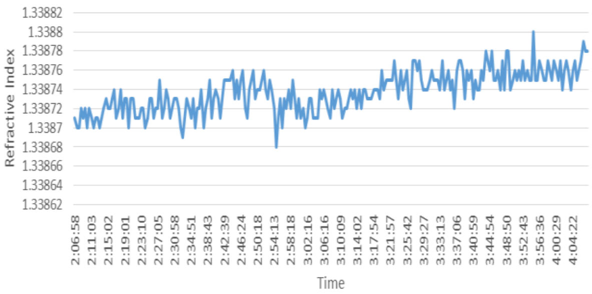

Fig.5. Measurement of refractive index of glucose/water solution at 20°C over 2 hours.

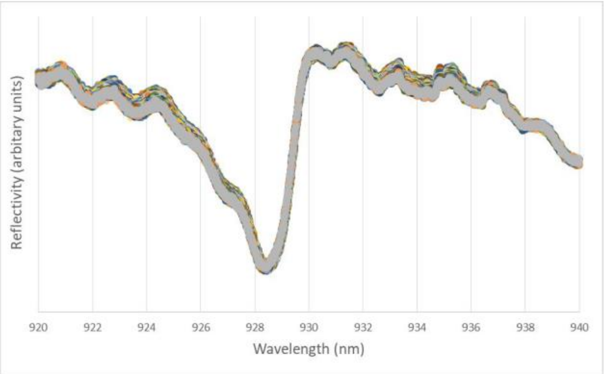

Fig.6. Stability test for the glucose/water solution for the 16EE sensor, over 2 hours.

From the figure 5, it can be seen that over 2 hours duration, the refractive index of glucose/water solution has varied about 0.00006 RIU, which is within the resolution range of the refractometer. Hence, the stability of refractive index is good for the next step, i.e. checking the stability of the resonance over 2 hours. The stability of resonance wavelength for the glucose/water solution is shown in figure 6 for the particular example of the 16EE sensor.

It can be clearly seen in figure 6 that, the resonance wavelength shows very good stability as the wavelength shift is only 0.02 nm over a long duration. So, my next step was to validate the reproducibility of my measurements on the same chip, using deionized water.

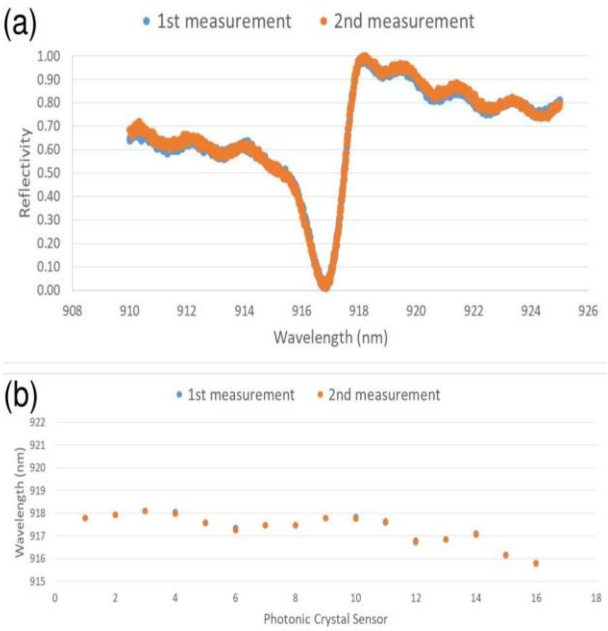

Fig.7. (a) Resonance spectrum for two consecutive measurements for the 13Y sensor in deionized water, and (b) overall resonance wavelength comparison along column Y.

Reproducibility Test: The reproducibility tests are systematically performed using deionized water as reference solution inside the liquid pool. As our chip has 32 identical rows with increasing resonance wavelength along a row and 32 columns where each column is composed of identical photonic crystals, I restricted my characterization to the measurement of the PhC reflectivity spectra along one complete row and one column (in my case row 16 and column EE). Then, the pool is emptied and the same procedure is performed again to determine whether or not exactly the same resonance shape and wavelength for the second attempt is achieved. Following this procedure for reproducibility study, I have observed no resonance shift between the two consecutive measurements, as overlapped spectrum for the 13Y sensor was found, which is shown in figure 7(a).

Again, if we observe the overall comparison for all the sensors along a whole column (here column Y), we see that there are no resonance shifts for almost all of the photonic sensors at all, and the spectra for the two consecutive measurements perfectly overlap. Figure 7(b) illustrates the overall resonance wavelengths comparison for reproducibility along the column Y.

The statistical analysis shows that, the average value of wavelength shift between two consecutive measurements is 0.005 nm and corresponding standard deviation is 0.0281 nm along column Y, which is a very strong indicator for the good reproducibility achieved with this particular chip. So, we can clearly say that, the measurements performed on this chip are reproducible and we can proceed to the sensitivity study, using a glucose/water solution with the same concentration.

Sensitivity Test: Figure 8 shows an example of resonance shift observed with the glucose/water solution (100 g/l) with respect to the reference in deionized water.

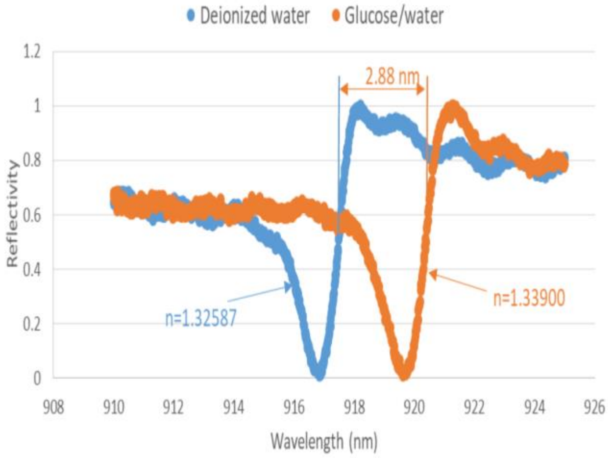

Fig.8. Resonance shift observed for glucose/water solution with respect to water, for the 13Y sensor.

From figure 8, we can see that the difference of refractive index between deionized water and glucose/water solution (0.0131 RIU) induces a 2.88 nm resonance shift, which corresponds to a sensitivity above 200 nm/RIU, as expected by the simulations for the CLIPO chips.

5. Conclusions

In our experiments, we have investigated the reproducibility, stability and sensitivity of measurements on the photonic chips. Reproducibility is the crucial factor for characterizing a sensor as the sensitivity and reliability of a sensor chip strongly depends on the reproducibility of the sensor responses. Good reproducibility is a validation of the experimental procedures (sample preparation and optical measurements) developed for the sensor characterization. Using deionized water as a reference solution, we have identified and eliminated the experimental cases yielding bad reproducibility, and then, for the cases with good reproducibility we have continued with sensitivity studies. We have found that for glucose/water solution, the CLIPO chips show good sensitivity compared to the state-of-the-art. Still, it needs more experiments, using solutions with different concentrations, to fully study and validate the sensitivity in glucose/water solution. The direct perspectives of this work will be the investigation of the surface sensitivity after immobilizing a protein (BSA) monolayer. In addition, we will perform a bio recognition test of streptavidin using biotin probes for the realization of real-time biomolecular screening. Thus as a general conclusion, we can say that, photonic crystal based biosensors represent a new class of advanced technology products that can be good candidates for a wide array of applications at the point-of-care diagnostics.

References

[1] Anthony P. F. Turner, “Biosensors: sense and sensibility”, Chem. Soc. Rev., 42, 3184, (2013).

[2] P. B. Luppa et al., “Point-of-care testing (POCT): Current techniques and future perspectives”, Trends in Analytical Chemistry, 30, 887, (2011).

[3] J. Homola et al., “Surface plasmon resonance sensors: review”, Sensors and Actuators B 54, 3, (1999).

[4] Joannopoulos JD, Johnson SG, and Winn JN, “Photonic Crystals: Molding the Flow of Light”, Princeton Univ Press, Princeton, (2008).

[5] Saeed Olyaee et al, “Photonic Crystal Chemical/Biochemical Sensors”, Progresses in Chemical Sensor, InTech, (2016).

Gold Nanoclusters on Nanoporous Anodic Alumina for Energy Storage Applications

Tabish Aftab, Josep Ferré i Borrull, Lluis F. Marsal

Eng. Electrònica, Elèctrica i Automàtica, Universitat Rovira i Virgili, Tarragona–43007, Spain
tabish.aftab@urv.cat, josep.ferre@urv.cat, lluis.marsal@urv.cat

Abstract

This work presents the fabrication of gold nanoclusters using electroless gold deposition on porous anodic aluminum oxide (AAO) template and demonstrates the electrochemical properties generated by the nanostructured gold surface. AAO membranes were prepared by electrochemical anodization of Al in 0.3 M oxalic acid electrolyte. Electroless gold deposition on AAO was performed via several steps using commercially available gold plating solutions. Scanning electron microscopy (SEM) images confirm that the gold nanoclusters formed onto AAO pores have characteristic nano clustered morphology as a result of the nucleation process during gold deposition. The electrochemical properties of gold deposited AAO will be tested by measuring cyclic voltammetry (CV), galvanostatic charge–discharge and impedance spectroscopy measurements

1. Introduction

The development of highly efficient energy storage and conversion systems is critical for addressing the crucial problems of climate change, limited availability of fossil fuels and environmental pollutions, and it also plays a key role inefficient utilization of sustainable and renewable energy (such as solar and wind energy). Currently, the research about energy storage and conversion is mainly focused on electrochemical energy storage devices (especially, supercapacitors and batteries) and solar energy conversion devices (mainly, photovoltaics and solar water splitting cells). Over the past decades, these energy storage and conversion (EESC) systems have witnessed their great advances and potential in many significant applications, e.g., portable electronics, electro-mobiles and smart power girds.

Unfortunately, the large-scale commercialization of these EESC devices is still hindered by their unsatisfied performances, including high cost, low power and energy density, insufficient durability, etc. In order to enhance these critical parameters to meet the practical applications, great efforts have been made to the rational design and fabrication of advanced nanostructured electrode materials with tailored structure, morphologies and compositions [1-2]. Among those nanostructures, ordered porous nanostructures are very promising and have been widely used in EESC systems. To fabricate ordered porous nanostructures, nanoporous anodic aluminum oxide (AAO) template offers an effective way due to its remarkable properties such as chemical and thermal stability, hardness, high surface area and versatility. Since the most significant progress in fabrication of highly ordered porous AAO template is dated long before, AAO templates have been extensively used over the past few decades, as an easy way to prepare a wide range of nanoarchitectures. The structure of porous AAO template can be described as a close-packed hexagonal array of parallel cylindrical nanochannels like honeycombs, ranging from 10 to 400 nm in diameter. The formation of the highly ordered hexagonal pore arrays is a self-organization process during the Al anodization by controlling anodization conditions, such as the type and concentration of the electrolyte, the applied voltage or the current, pH value, anodization duration and temperature, etc. Energy storage systems such as Supercapacitors have also attracted significant attention in that they are more advantageous than batteries in terms of their higher power density and more excellent cyclability. Besides, they can act as the bridge for the power/energy gap between traditional dielectric capacitors (having high power output) and batteries/fuel cells. Similar to batteries, it consists of two electrodes, a separator and the electrolyte. Charges can be stored and separated at the interface between the conductive electrodes (e.g., carbon-based materials or metal oxides) and the electrolyte [3-4].

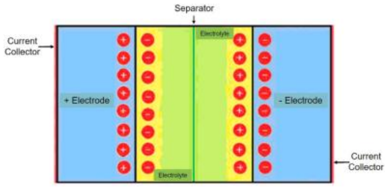

Fig. 2: Schematic diagram of an electrochemical supercapacitor.

AAO template plays a pivotal role to achieve high power capabilities for supercapacitors. Here we synthesized highly porous AAO templates which will further processed by electroless deposition of gold nanoclustures and these Au@AAO templates were investigated extensively as an electrode material for high performance supercapacitor.

2. Experimental Description

AAO substrate was fabricated by two-step electrochemical anodization using aluminum plate. Aluminum plates with thicknesses of 2 mm were cut of size 2×2 cm. They were cleaned with acetone, and then rinsed twice in deionized water. For pretreatment, electropolishing was applied at 10◦C under 12 V for 4 min in a 1:4 mixture of perchloric acid and ethanol through continuous stirring to remove the natural oxide layer from the surface. After the electropolishing, one step anodization was performed on the Al surface by using an 0.3 M oxalic acid solution at 5◦C and 40 V for 20h. Afterwards, the samples were etched chemically in 1 M phosphoric acid for 90 min at 70◦C. The second anodization, which controls the depth of pores, was performed upto 48 coulomb charge deposition for a depth of 1000nm. The diameter of the pores Dpo: 20-30 nm is usually formed by 0.3 M oxalic acid solution. The pore diameter was determined using SEM.

Gold nanoclusters were deposited by immersing AAO plates in 1.25 mM of auric chloride in an aqueous solution at room temperature. The plates were washed with deionized water several times and dried with N2 gas. The UV–vis absorbance measurements of the finally obtained AAO samples confirmed the deposition of nanoclusters and also the AAO surfaces were examined with SEM.

3. Results and Discussion

The SEM image of AAO layer is shown in Fig. 3a. The pore diameter of AAO was measured from the SEM image as 20-30 nm. After immersing AAO in the 1.25 mM of gold solution for 1h, aggregated gold nanoparticles with sizes ranging from 50 nm to 150 nm and sphere-shaped gold clusters were observed on the AAO as shown in figure 3b.

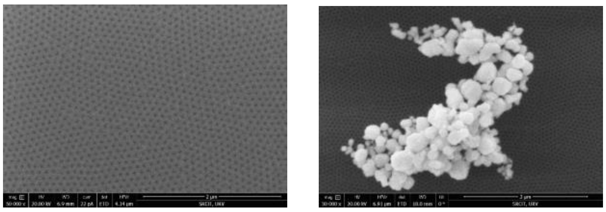

Fig. 3: SEM images (a) Nanoporous anodic alumina AAO, and (b) gold nanoclusters on AAO

Gold Nanoclusters are also confirmed by UV-vis absorbance spectroscopy. The absorption maximum is at 560 nm (fig. 4). The broadness of the peak is due in part to the distribution in particle size (10±5 nm).

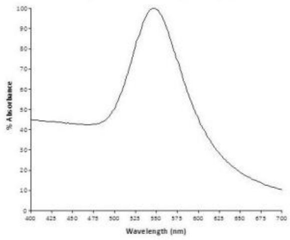

Fig. 4: UV-Vis. Spectra of gold nanocluster on AAO substrate

These obtained AAO substrates can be used as an electrode for the fabrication of supercapacitor. Two such films can be bonded back-to-back make a single supercapacitor device. The Au segment of each electrode remains in contact with the Cu layer acts as the current collector. The electrochemical properties and capacitive behaviour of the supercapacitor electrodes will be studied by cyclic voltammetry (CV), galvanostatic charge–discharge and impedance spectroscopy measurements. The specific capacitance will be calculated from galvanostatic charge–discharge measurements. In order to compare the supercapacitor performance of our Au@AAO hybrid electrodes with simple two Al-electrode supercapacitor, electrochemical measurements will also be carried out for the supercapacitor devices with AAO template-grown electrodes where a thermal evaporated metal layer act as the current collector.

4. Conclusions

In this work we have discussed the fabrication of nano porous anodic alumina by 2- step process using oxalic acid as electrolyte. Using electroless deposition, gold nanoclusters were deposited onto the surface of alumina. It has also been proposed that this gold deposited AAO can be used as an electrode for supercapacitor. The electrochemical properties will be tested by cyclic voltammetry (CV), galvanostatic charge–discharge and impedance spectroscopy measurements to measure the performance of the supercapacitor.

References

1. Zhao, Huaping, Min Zhou, Liaoyong Wen, and Yong Lei. "Template-directed construction of nanostructure arrays for highly-efficient energy storage and conversion." Nano Energy 13 (2015): 790-813.
2. Hornyak, Gabor, Michael Kröll, Raphael Pugin, Thomas Sawitowski, Günter Schmid, Jan-Olov Bovin, Gunnel Karsson, Herbert Hofmeister, and Sigrid Hopfe. "Gold clusters and colloids in alumina nanotubes." Chemistry–A European Journal 3, no. 12 (1997)
3. Tezcan, Tuğba, and Ismail Hakki Boyaci. "A new and facile route to prepare gold nanoparticle clusters on anodic aluminium oxide as a SERS substrate." Talanta 232 (2021): 122426.
4. Suongá Ou, Fung. "Synthesis of hybrid nanowire arrays and their application as high-power supercapacitor electrodes." Chemical communications 20 (2008): 2373-2375.

Numerical approach to input filter design for switching converters

Ramon Estalella, Angel Cid, Carlos Olalla

Universitat Rovira i Virgili

1. Introduction

The design of power filters is an important part of the design of switching power converters. These converters often require input filters to reduce current and voltage ripple and to comply with conducted electromagnetic interference (EMI) regulations. Since input filters are typically designed on top of existing converters, designers must consider the possible interactions that may arise. Such interactions can not only make a switching converter lose some of the dynamic performance but even make it unstable.

The basis for what can be considered a conventional design can be seen on [1]–[3]. It typically relies on simplifications of the stability criteria that might lead to conservative results.

This paper aims to develop a numerical tool that may aid in the design process. The tool finds a parameter region that ensures design criteria, stability and pole placement conditions. Then the designer can choose appropriate components within that region, according to other restrictions such as size, cost, space, fitting to commercial values, etc.

2. Numerical Tools Employed

The investigation of the domain of stability that we propose is based on a convex combination of Lyapunov functions, following the ideas in [4]. The use of parameter-dependent Lyapunov function provides some degree of flexibility, and therefore the results are less conservative compared with the single Lyapunov function approach.

The dynamical characteristics of the system to be designed can be specified by pole placement techniques. It is possible to relate the maximum natural frequency of oscillation of the poles of a system to a circle in the complex plane centered at the point $0 + 0j$ with radius ρ. The LMI conditions that verify the location of the poles of the system in a generic circular region have been derived in [5].

The damping ratio can be enforced by keeping the poles inside a conic region of angle θ such that $\theta = cos^{-1}(\zeta)$. Starting with the θ condition presented on [6] and following a similar procedure to the one described on [4] for the stability LMI it is possible to obtain the pole placement LMIs required to ensure a specified θ implemented with parameter-dependent Lyapunov functions. The shape of the final pole placement region can be seen on Fig. 1. As stated in the introduction, the proposed algorithm does not return a single parameter value, but rather a region or a domain of values. As in [4], [5], consider the following continuous-time linear system:

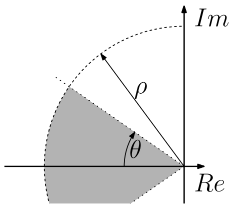

Figure 1: Region defined with the pole placement LMIs.

$$\dot{x}(t) = \left(A_0 + \sum_{i=1}^{m} \alpha_i E_i \right) x(t) \qquad (1)$$

where $x \in \mathbb{R}^n$, $A_0 \in \mathbb{R}^{n \times n}$ is the nominal matrix of the system, $E_i \in \mathbb{R}^{n \times n}$ $(i = 1, ..., m)$ are given matrices representing the perturbation directions and $\alpha_i \in \mathbb{R}$ $(i = 1, ..., m)$ are scalar values defining the amount of perturbations allowed.

The α_i will be increased by means of two algorithms. Algorithm 1 will be a modified bisection algorithm which will aim to search for a weighted region of parameters given an initial feasible point. Fig. 2 gives a visual representation of how it works.

Algorithm 2 will be used to iteratively find the next initial point (A_{new}) towards the desired direction of movement (in accordance to some factors such as size, cost, etc.) It will keep using the Algorithm 1 in order to get new feasible and usable regions closer to the "ideal" parameters. Fig. 3 shows one of the steps (going from an initial A_0 to a better A_{new}.

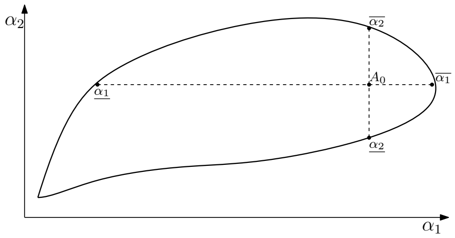

(a) Maximum independent non-symmetric domain example.

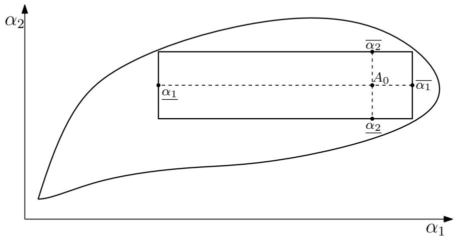

(b) Simultaneous non-symmetric domain example.

Figure 2: Bisection algorithm domains examples

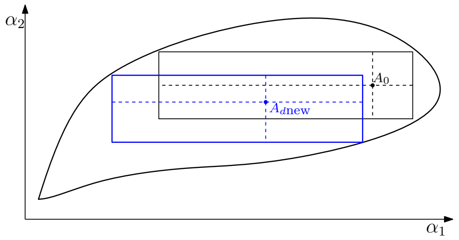

Figure 3: Example of the domain obtained by the bisection algorithm with A_0 and the domain obtained with $A_{d\text{new}}$.

3. Example: LC Filter with Parallel LR Damping Branch

In this filter topology, shown in Fig. 4, the aim is to reduce the filter parameters while being able to obtain a parameter region from which a designer can extract viable filter parameters. The damping is given by a L-R branch in parallel with the filter inductance. The losses are low since the DC power does not involve the damping resistor. Table 1 shows numerical values tested for this type of filter, including the initial values from which Algorithm 2 has started, the resulting range of filter parameters and finally a possible filter option.

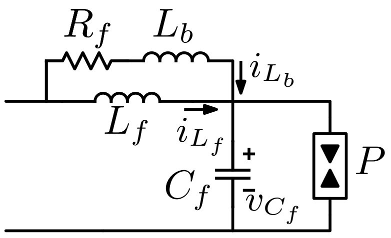

Figure 4: LC filter with parallel R_f and L_b branch, loaded by a CPL.

	Initial values	Parameter ranges	Values selection
L_f	500 μH	$7.82 - 246e6\ \mu H$	10 μH
C_f	100 μF	$21.3 - 83.4\ \mu F$	33 μF
L_b	150 μH	$1.96 - 2.91\ \mu H$	2.2 μH

Table 1: LC with parallel RL branch numerical example

4. Conclusions

This paper presents a numerical approach to physical parameter selection by means of uncertain models. LMIs have been used to implement performance conditions which force a minimum attenuation and damping of the system. A modified bisection algorithm has been used in order to find a region of parameters compatible with the performance conditions. It has been shown that it is possible to start with large parameters and iterate to find parameter regions with smaller overall parameters until certain tolerance conditions are met.

References

[1] R. W. Erickson and D. Maksimovic, *Fundamentals of Power Electronics 2nd Edition*. 2008, ISBN: 0306480484. DOI: `10.1017/CBO9781107415324.004`. arXiv: `arXiv:1011.1669v3`.

[2] R. D. Middlebrook, “Input Filter Considerations in Design and Application of Switching Regulators,” *IEEE Industry Applications Society Annual Meeting*, pp. 366–382, 1976.

[3] R. D. Middlebrook, “Design Techniques for Preventing Input Filter Oscillations in Switched-Mode Regulators,” *Proceedings of Powercon 5*, A3.1–A3.16, 1978.

[4] D. C. Ramos and P. L. Peres, “An LMI approach to compute robust stability domains for uncertain linear systems,” *Proceedings of the American Control Conference*, vol. 5, no. 2, pp. 4073–4078, 2001, ISSN: 07431619. DOI: `10.1109/ACC.2001.946351`.

[5] V. J. Leite, V. F. Montagner, and P. L. Peres, “Robust pole location by parameter dependent state feedback control,” *Proceedings of the IEEE Conference on Decision and Control*, vol. 2, no. December, pp. 1864–1869, 2002, ISSN: 01912216. DOI: `10.1109/cdc.2002.1184796`.

[6] M. Chilali and P. Gahinet, “H_inf Design with Pole Place Constraints: An LMI Approach,” *Ieee Transactions on Automatic Control*, vol. 41, no. 3, pp. 358–367, 1996.

Custom backscatter modulation based on CSS signals with an enhanced processing gain

M. Lazaro*(1), A. Lazaro(1), R. Villarino(1), and D. Girbau(1)

(1) Department of Electronics, Electrics and Automatic Control Engineering, Rovira I Virgili University, 43007, Tarragona, Spain, Email: marc.lazaro@urv.cat

Abstract

This work presents an improved backscatter tag based on double gain modulation. This research aims to increase the backscatter range without compromising power consumption. To do this, a chirp spread spectrum (CSS) modulation is used to illuminate the tag. The idea behind this work is to bounce incoming CSS signals by modulating the switching frequency of the tag with a down-chirp of identical bandwidth and duration as the incoming signal, resulting in the reflection of a constant frequency signal with significant processing gain. An On-Off keying (OOK) modulation is used to encode the tag information. In addition, a Barker sequence is used to further improve the detectability of the tag, providing an additional processing gain on the receiver side.

1. Introduction

The main barrier to further spreading IoT wireless nodes worldwide is power consumption. The ability to reduce that consumption will bring about a wide amount of new possible applications and give a boost to the IoT market. At the same time, the relentless reduction in power consumption of microcontrollers puts the spotlight on radio frequency circuits, which use energy-hungry power amplifiers. The objective is to help provide IoT devices with wireless capabilities without increasing energy consumption at several milliamperes.

This work studies the use of the backscattering technique to solve the aforementioned issue. It can be used with any modulation, but recently backscattering tags based on bouncing chirp spread spectrum (CSS) modulations have attracted great interest due to their outstanding performance. LoRa is a CSS-based modulation that stands out for a set of features suitable for IoT applications. The most noteworthy are the long-range radio links and the robustness to interferences. Long distances are achievable as a result of the excellent sensitivity of LoRa receivers, down to -148 dBm.

The main drawback of the backscattering is the trade-off between power consumption and the bounced signal strength, which is abruptly reduced. To deal with that, a novel tag modulation that increases the power of the scattered signal -and consequently the range- is proposed.

2. Operation Principles

In backscatter communications, conventional radio transceivers are removed from the tag. Therefore, backscatter devices use signals from the environment as carriers to bounce them with new information. Any of the usual communication systems (BLE, Wi-Fi, etc.) can be used as a carrier, or if necessary, as will see in the following sections, any other type of transmitter can be installed to also be used as a carrier. This technique replaces standard radio-frequency circuitry with an RF switch with a power draw of less than a microamp, dramatically increasing the battery life of the tag or even allowing us to create a battery-less tag.

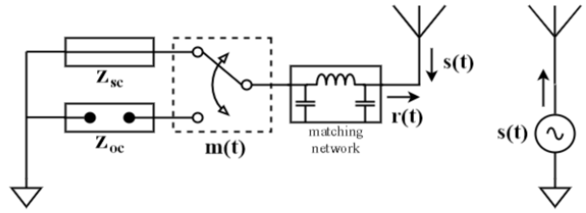

Fig. 1. Equivalent circuit of the backscatter technique.

The theoretical basis behind this technique has been well established in the literature [5][6]. The amplitude of the backscattered signal depends on the differential radar cross-section (RCS) of the tag, which in turn depends on the reflection coefficient generated by the impedances loading the antenna. To maximize the RCS of the tag, the antenna load is typically switched between a short circuit and an open circuit. Fig. 1 represents the equivalent circuit of the backscattering tag, where Z_{SC} and Z_{OC} represent the short circuit and open-circuit impedances, respectively, *m(t)* is the modulating signal that controls the switch, *s(t)* is the ambient carrier signal, and *r(t)* is signal reflected by the tag.

As mentioned, the backscattered signal is weaker than the incoming signal and consequently is hidden behind it. If we modulate *m(t)* at a frequency higher than the bit period, we can shift the reflected signal to the sidebands, avoiding this hiding effect. Therefore, by modulating the signal *m(t)* with a sinusoidal or a square signal of frequency f_{OSC}, the signal scattered by the tag is transmitted to $f_C \pm f_{OSC}$. Considering that the switching frequency has a duty cycle of *50%*, the differential *RCS* of the antenna can be obtained by:

$$\Delta\sigma = \frac{\lambda^2}{4\pi} \cdot G^2 \cdot |\Gamma_{SC} - \Gamma_{OC}|^2 \cdot M$$

where M is the modulation factor that is a function of the first Fourier coefficient of the modulating waveform (e.g. squarewave).

3. Modulation Description

To compensate for the weakness of the backscattered signal, a novel solution to increase its detectability is proposed. The modulation described in this section stems from the demodulation process used in the LoRa modulation. LoRa encodes information circularly shifting the base chirp, which starts at f_0 and finishes at f_0 + BW. To demodulate the transmitted chirps, the receiver multiplies the incoming signal by a complex conjugate time-reversed chirp with the same bandwidth and period as the incoming chirp. The signal resulting from this operation is a complex sinusoid signal with a great processing gain.

The idea presented in this article lies in directly modulating the switching frequency of the tag *m(t)* with the aforementioned down-chirp signal, consequently bouncing a complex sinusoidal signal. The result of this operation is a frequency tone whose amplitude concentrates the spread power of the incoming signal, achieving an extra gain of 13 dB, compared to the conventional backscattering process. Fig. 2 illustrates the gain of the down-chirp modulated backscatter over the constant frequency-modulated backscatter using a CSS signal as an incoming signal. For the experiments, the bandwidth (BW) and the spreading factor (SF) of the chirp were set to 125 kHz and 12.

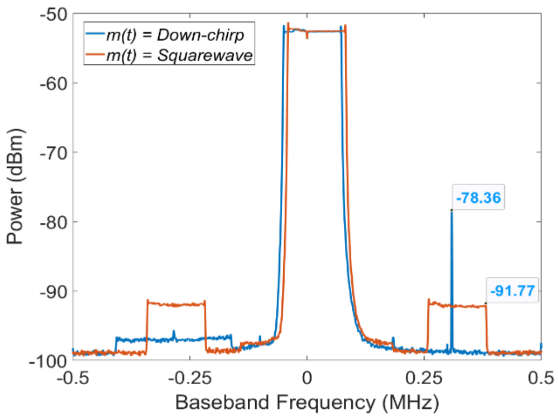

Fig. 2 Spectrum comparison between conventional backscatter and down-chirp modulated backscatter. Source signal: CSS modulation (Up-chirp), f_c = 868 MHz, BW = 125 KHz and SF = 12. Conventional Backscatter signal (Orange): Squarewave, f_c=300 kHz, duty cycle = 50%. Down-chirp backscatter signal (Blue): CSS modulation (Down-chirp), f_c = 300 kHz, BW = 125 KHz and SF = 12.

Data is encoded using an OOK modulation. A digital one is transmitted when m(t) is modulated with a down-chirp and a frequency tone is backscattered. On the contrary, cutting off the modulation m(t) nothing is bounced, which is equivalent to a digital zero. At this point, information could already be sent. However, to further increase the detectability of the tag, it is proposed to use a Barker sequence to encode the information and provide a second processing gain to the system. Fig. 3 shows the reflected signal and the tag data encoded with the Barker sequence.

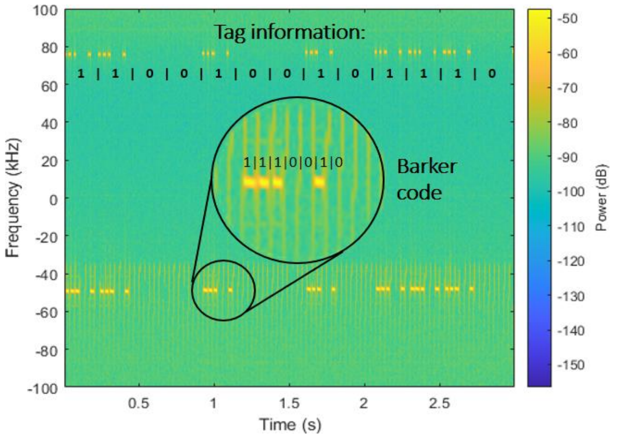

Fig. 3 IQ recording of the backscattered signal encoded with the 7-bit barker sequence.

5. Conclusions

Backscatter is the alternative to conventional radios for low data-rate, low-power IoT applications. In this work, a double processing gain method to enhance conventional backscatters and counteract their range deficiency is proposed and tested. The first processing gain comes from backscattering a frequency tone as a result of modulating the tag with a downward chirp when an upward chirp illuminates the tag. The second processing gain is on the receiver side and consists of sending the tag information with an OOK modulation using a Barker sequence. Finally, the range achieved with a preliminary version of the tag, setting the transmitter power at 20 *dBm*, is about 20 meters, similarly to Wi-Fi and Bluetooth communications.

References

[1] Niu, J. P., Li, G. Y. (2019). An overview on backscatter communications. Journal of Communications and Information Networks, 4(2), 1-14.

[2] Lazaro, A., Lazaro, M., & Villarino, R. (2021). Room-level localization system based on LoRa backscatters. IEEE Access, 9, 16004-16018.

[3] Li, H., Tong, X., Li, Q., & Tian, X. (2020, December). Xorlora: Lora backscatter communication with commodity devices. In 2020 IEEE 6th International Conference on Computer and Communications (ICCC) (pp. 706-711). IEEE.

[4] Nikitin, P. V., Rao, K. V. S., & Martinez, R. D. (2007). Differential RCS of RFID tag. Electronics Letters, 43(8), 431-432.

[5] LoRa Modulation Basics. AN1200.22, May 2015.

Development of a novel carbonized porous silicon electrochemical sensing platform by pyrolysis of furfuryl alcohol

Anandapadmanabhan A. Rajendran[1], Keying Guo[4], Marina Bujaldon Velasco[1], Kandeel Shafique[1], , Pilar Formentín[1], Hedieh Haji-Hashemi[1], Nicolas H. Voelcker[5 6 7], Xavier Cetó[2], Beatriz Prieto-Simón*[1, 3]

[1] Department of Electronic Engineering, Universitat Rovira i Virgili, 43007 Tarragona, Spain
[2] Department of Chemistry, Universitat Autònoma de Barcelona, 08193 Bellaterra, Spain
[3] ICREA, Pg. Lluís Companys 23, 08010, Barcelona, Spain
[4] Biological and Environmental Science and Engineering Division, King Abdullah University of Science and Technology, Thuwal, Saudi Arabia
[5] Faculty of Pharmacy and Pharmaceutical Sciences, Monash University, Parkville, V IC, Australia
[6] Melbourne Centre for Nanofabrication, Victorian Node of the Australian National Fabrication Facility, Clayton, V IC, Australia
[7] CSIRO Manufacturing, Clayton, V IC , Australia
beatriz.prieto-simon@urv.cat

Abstract:
Over the years, porous silicon (pSi) has emerged as a promising material, especially in sensing applications, due to its advantageous properties such as a large surface area (>100 m^2/cm^2), ease of functionalization, tuneable pore size (from a few nm to several µm), thickness (from a few nm to the silicon wafer thickness) and porosity. Such features can be easily tuned by simply changing the etching conditions to tailor the desired application needs. Precisely, thanks to its tuneability and versatile surface chemistry, pSi allows the incorporation of a wide range of functionalities for the covalent immobilization of diverse biomolecules as bioreceptors, thereby serving as a perfect tool for biosensing purposes. However, its use as an electrochemical transducer is limited by the chemical instability of hydride terminated freshly etched pSi, that are prone to oxidation. Thus, surface modification of pSi is crucial for its stabilization, while at the same time for crafting desired functional groups on its surface to immobilize various recognition elements.

Herein, we propose the polymerization and carbonization of furfuryl alcohol (PFA) on pSi to get a carbon-stabilized pSi device, featuring a conductive layer as a suitable nanostructured electrochemical transducer. The freshly etched pSi wafers are modified with furfuryl alcohol (FA) by spin coating and later subjected to thermal heating for the carbonization of FA. Morphological features of synthetized PFA-pSi were extensively studied using Field Emission Scanning Electron Microscopy, while Fourier-transform infrared spectroscopy was used to investigate the surface chemistry. Electrochemical characterization using cyclic voltammetry, electrochemical impedance spectroscopy were used to demonstrate the electrochemical performance and stability of PFA-pSi.

Finally, the potential of such platform for electrochemical (bio)sensing applications was underpinned by the development and optimization of a PFA-pSi based biosensor for the detection of bacterial 16SrRNA from *Staphylococcus aureus*. Hence the excellent electrochemical performance of this platform along with its versatile surface chemistry highlights its potential to be used as a novel nanostructured electrode for electrochemical sensing applications.

Keywords: Porous silicon, carbon-stabilization, polyfurfuryl alcohol, electrochemical biosensor

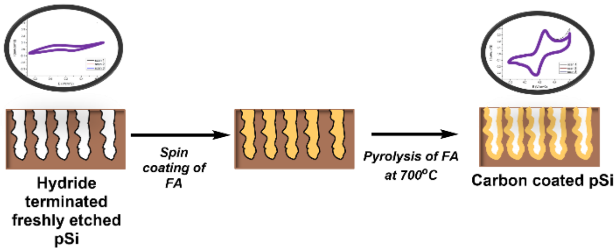

Figure 1: Stepwise carbonization of freshly etched pSi using furfuryl alcohol

References:

1. Guo, K., Sharma, A., Toh, R. J., Alvárez de Eulate, E., Gengenbach, T. R., Cetó, X., ... & Prieto-Simón, B. (2019). Porous silicon nanostructures as effective faradaic electrochemical sensing platforms. Advanced Functional Materials, 29(24), 1809206.
2. RoyChaudhuri, C. (2015). A review on porous silicon based electrochemical biosensors: Beyond surface area enhancement factor. Sensors and Actuators B: Chemical, 210, 310-323.

LoRa: A Suitable Wireless technology for Wearable Devices in salt-water Environments

Elouan Thierry[1], Alejandro Santos[2], Alfonso Romero[2], José Luis Ramirez[2]

[1] University of Bordeaux, Talence, France. emal: elouan.thierry@etu.u-bordeaux.fr, phone: +33749664367
[2] Minos, Departament d´Enginyeria Electrònica Elèctrica i Automàtica, Universitat Rovira i Virgili, Tarragona, Spain.

Abstract

LoRa wearable devices have found numerous applications to monitor fitness and healthcare. Usually, this kind of portable devices can go with their carrier everywhere, but they can behave differently according to the outside environment. Establishing a wireless communication in a salt-water environment is not easy to achieve. Indeed, when the water has a high concentration of salt, the liquid is very conductive, and this result in a strong attenuation of the electromagnetic waves. In this work, we studied the performance of LoRa technology in a seawater simulated environment. We were also interested in the behavior of the signal and the power consumption of the devices, also predicted the devices´ autonomy using different capacities-batteries.

1. Introduction

Nowadays, underwater communications are becoming increasingly important as they are useful in many fields. They allow the development of devices to control water pollution, predict natural disasters and military applications [1]. However, establishing communications in a saline environment is not easy because this medium is highly conductive and causes strong attenuation of electromagnetic waves [2]. To be able to transmit information and reduce attenuation, the frequency bands must be very low [3, 4] and a very high transmission power is required [1]. However, it will result in a high-power consumption, reducing the autonomy of the devices [5]. Additionally, the autonomy of the devices is an important parameter for developing applications in environments that are difficult to access such as the ocean [6].

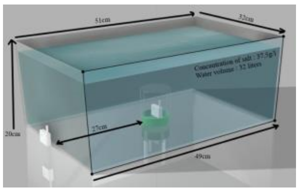

Fig.1. Setup of the experiments.

Regardless to LoRa technology, some work has been done to test LoRa performance in different environments, particularly over seawater [7]. Besides, LoRa has been rising as a cutting-edge technology for wearable devices. A lot of studies have been developed to prove how suitable is LoRa for newest wearable devices [8-12]. This work studies the performance of LoRa in a salt-water simulated environment. Thus, LoRa is a suitable technology for develop new wearable devices in salt-water environment.

2. Tools and Methods

LoRa Transmitter (LoRaTx) and LoRa Receiver (LoRaRx): The ESP32 Wifi LoRa V2 [13] and the ESP32 Wireless Sticklite [14] were used to transmit the data and perform different communication tests using a point-to-point (P2P) connection.

Module sealing: The LoRaTx was immersed in a salt-water solution to perform the communication. To do so, a cylindrical plastic bottle with a screwcap was used and the neck was wrapped with Teflon. Afterwards several layers of PVC-tape were added around the screwcap to seal the bottle. Using this method, the transmitter was put at a depth of 15 cm for a working day time without having any issue. Figure 1 shows a diagram of the setup.

Power Consumption: The Keysight Quick IV Measurement Software and the Keysight B2902A Precision Source Measure Unit were used to acquire the power consumption of the modules. A comparison between LoRa normal mode and deep-sleep mode was made to understand its impact in the power consumption. Also, parameters of the physical layers of LoRa were fixed at minimum during the measurements such as: spreading factor, coding rate and the bandwidth. These parameters have an impact in the device autonomy, the sensitivity of the LoRaRx, the bit rate and the time on the air indicator. [15]

3. Influence of salt on LoRa

To obtain the receiver signal strength indicator (RSSI), a firmware was designed and set into the LoRaRx. The values of the RSSI were obtained while increasing the salinity of the water. To do so, the LoRaTx was placed in a waterproof box and then in the plastic container with 32 liters of water. Having 27 cm line of sight (LoS) between LoRaTx and LoRaRx. Figure 1. Afterwards, 100 grams of salt was added in each step-measurement, having a variation of the salinity from 0 to 37,5 g l^{-1} [16]. In this case, during each step of salt-increasing although the RSSI got a deterioration, LoRa communication was successfully established, and no packet loss was detected. Subsequently, having the idea of decrease the current consumption, the connection was yet established fixing the level of salinity at 37.5 g l^{-1} and making some variation of the power transmission (PTx), between 14 and 4 dBm [17], Figure 2 shows RSSI as a function of PTx: (i) Yellow RSSI: LoRaTx outside the salt-water. (ii) Blue RSSI: LoRaTx inside the salt-water. As expected, the RSSI is better when the LoRaTx is out of the water. However, even though the signal strength is weak when the transmitter is inside the salt-water; P2P connection was always established.

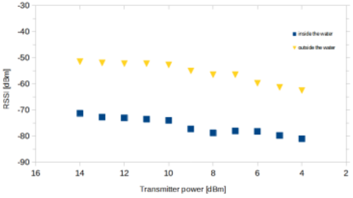

Fig.2. RSSI as a function of the transmission power.

4. Current consumption

The power-performance of LoRa is evaluated setting all the parameters of the physical layer at minimum to decrease the current consumption [15]. Figure 3 shows 1 packet/min of LoRa connection for 75 seconds. The deep-sleep mode was activated, having the mean of current = 45 mA (normal mode) and 2.6 mA (deep-sleep mode).

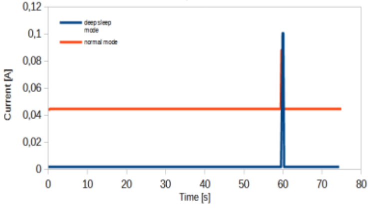

Fig.3. Current consumption of a LoRa (1 packet/min).

On the other hand, Figure 4 shows how increasing the time between transmissions from every min to every 5 mins drops the mean of current consumption in deep-sleep mode from 2.6 mA to 1.93 mA, respectively (25.77 %). As the time between transmissions increases, the mean of current consumption drops near to the mean of current consumption in deep-sleep mode. For example: the difference of the current consumption between sending 1 packet/hr (1.77 mA) and 1 packet/day (1.76 mA) is shorter (0.56 %) than the variation mentioned above. Figure 5 shows the autonomy of the device as a function of the capacity of the battery (deep-sleep mode) making some variation of the time between transmissions. As discussed before, the difference between sending a 1 packet/hr and 1 packet/day is not relevant related to current consumption. But is quite relevant related to the quantity of data that can be sent. One packet/hr has an increase of 2300 % of data compared to 1 packet/day. So, using 1 packet/hr and an 8800 mAh capacity battery will increase the quantity of data and the autonomy of the device around 200 days.

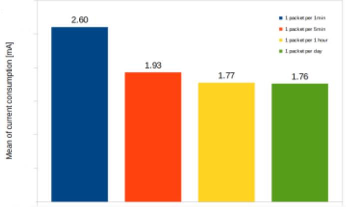

Fig.4. Mean of current consumption.

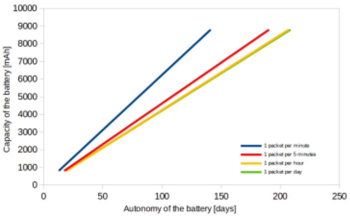

Fig.5. Devices autonomy according to the battery capacity.

5. Conclusions

Increasing the salinity from 0 to 37.5 g l^{-1} decreases the RSSI in ≈ 38 % (distance LoS = 27 cm). Even if the amount of salt is significant, it is possible to establish LoRa P2P communication. Physical layer parameters of LoRa and the PTx can be reduced at minimum to increase the autonomy of the device around 200 days (using 1 packet/hour and 8800 mAh of capacity battery). This is an ongoing project and there are some others tests to perform, but so far, LoRa is a suitable technology for the develop of new wearable devices in salt-water environments.

References

[1] Nejah Nasri, et al. Étude de l'architecture d'un réseau de communication Aquatique Sans Fils ", January 2007.
[2] Evangelia K., Electromagnetic Waves under Sea: BowTie Antenna Design for Wi-Fi Underwater Communications, January 2015.
[3] Hemani-Kaushal et al. Underwater Optical Wireless Communication. April 29, 2016.
[4] Joseph T., China's NYC-Sized 'Earthquake Warning System Array Sounds More Like a Way to Talk to Submarines. Dec 31, 2018.
[5] E Baumker, et al, “Minimizing power consumption of LoRa® and LoRaWAN for low-power wireless sensor nodes”,2018.
[6] Ao Huang, et. al. “A Practical Marine Wireless Sensor Network Monitoring System Based on LoRa and MQTT”, 2019.
[7] Nikola Jovalekic, et. al. Experimental Study of LoRa Transmission over Seawater, 29 August 2018.
[8] Yashash Jain, et al. Novel wearable devices for Health Monitor and Tracking of soldiers Based on LoRa Module.
[9] Gaby Bou Tayeh, et al. A Wearable LoRa-Based Emergency System for Remote Safety Monitoring.
[10] Urja Kulkarni, et al. Implementation of Backtracking Algorithm for navigation in LoRa-enabled wearable device for Dementia patients. 2020 IEEE 5th International Conference on Computing Communication and Automation (ICCCA) Galgotias University, Greater Noida, UP, India. Oct 30-31, 2020.
[11] L.H. Trinh, et al. Low-profile horizontal omni-directional antenna for LoRa wearable devices. 2017 International Conference on Advanced Technologies for Communications.
[12] Fan W., et al. WE-Safe: A Self-Powered Wearable IoT Sensor Network for Safety Applications Based on LoRa.
[13] ESP32 WiFI LoRa V2. https://heltec.org/project/wifi-lora-32/
[14] Wireless Stick lite. https://heltec.org/project/wireless-stick-lite/
[15] Marco C., et al. An Experimental Evaluation of the Reliability of LoRa Long-Range Low-Power Wireless Communication, June 2017.
[16] Dr. Nasreen, “Ocean Salinity, 15 January 2022
[17] https://www.thethingsnetwork.org/docs/lorawan/regional-parameters/

Nine-level PV-fed Cascaded H-Bridge Inverter Operating As a Shunt Active Power Filter

Seyedamin Valedsaravi*, Abdelali El Aroudi†, and Luis Martinez-Salamero‡
*seyedamin.valedsaravi@urv.cat, †abdelali.elaroudi@urv.cat, ‡luis.martinez@urv.cat

***Abstract*—Active Power Filter (APF) is a promising solution to eradicate harmonics pollution in future power grids with high penetration of nonlinear loads, including power electronic converters, diode-rectifiers, arc furnaces, and electrified railways. A cascaded H-Bridge (CHB) inverter could be a desirable APF in medium and high voltage systems thanks to its low switching frequency. Grid-connected Photovoltaic (PV) systems have inherently potential to be also APF. The only challenge is to add APF functionality to the control of grid-connected inverters. To aim that, in this paper, the control of a grid-connected 9-level CHB shunt APF is addressed in presence of nonlinear loading conditions. The system consists of PV arrays, DC-DC boost converters, DC-link capacitors, and CHB inverter. The boost converters control objective is to track maximum available power from the PV sources. The DC-link capacitors are used to decouple the AC and DC network dynamics. Moreover, the control objective of the CHB is to deliver the power in phase with the Point of Common Coupling (PCC) voltage as well as compensating nonlinear load harmonic current with synchronous reference frame (SRF) theory. Low Pass Filter (LPF) is used to smoothly determine the active component of the inverter output current. Proportional resonant controller is used for the CHB current control loop. The performance of the 9-level CHB shunt APF under irradiance and load change conditions is validated through numerical simulations performed on PSIM© software.**

***Index Terms*—Active power filter, 9-level cascaded H-bridge inverter, Grid-connected, Synchronous reference frame, Photovoltaic.**

I. INTRODUCTION

Power electronic converters are nonlinear and they can create harmonic pollution in the power system. Other sources of harmonic pollution are nonlinear loads, such as diode-rectifiers, arc furnaces, electrified railways, and frequency control devices which are recently increasingly used in the power grids. Harmonic pollution may endanger safe and stable operation of a power system. Active power filters (APFs) attract more attention in industrial applications. They can be connected to the power grid in shunt for harmonic current compensation and in series for harmonic voltage suppression. Since photovoltaic (PV) systems are connected to the power grid through a DC-link and an inverter, they inherently have the potential to be APFs. Therefore, the control of a grid-connected PV system can change to twofold aims. The first one is to deliver the maximum power to the grid with high power quality satisfying standards such as IEEE [1] and the second one is to compensate nonlinear local load harmonics and reactive power.

II. SYSTEM DESCRIPTION

Fig. 1 shows the circuit diagram considered in this paper. The CHB inverter consists of four half-bridge cells with four switches in each module. Therefore, the output voltage would be 9-level. Four boost converters performing MPPT control are used to deliver maximum available power from the PV sources to the main grid. In order to decouple the DC and AC system dynamics, four DC-link capacitors are used between CHB and the boost converters. A passive LC filter is installed in the output of CHB to decrease switching harmonics injection. The nonlinear load involving full-wave bridge rectifier, series resistor, and inductor is located in parallel at the point of common coupling (PCC). The whole system is connected to the main grid through the PCC.

III. SYSTEM CONTROL

The control of the considered system has four stages including MPPT control of PV sources, shunt APF control, grid synchronization, and PWM control of the switches. These stages are detailed in this section. The system works as a shunt APF and provides harmonic and reactive power; thus, a more number of modules can prevent oversizing of the H-bridges and their switches.

A. Shunt CHB Control

In the shunt CHB control, three important injected current components should be determined for the inverter current reference i_2^* determination. These are the peak amplitude of the injected grid current i_{DC}, the capacitor DC current charging i_{DC}^*, and the harmonic component of load current i_{Lh}. In terms of these components, the current reference i_2^* can be expressed as follows

$$i_2^* = (i_{DC} - i_{DC}^*)\sin(\omega_g t) + i_{Lh} \tag{1}$$

1) Active power component: The grid current active power component is related to the maximum available power from the PV sources

2) DC-link control component: For the stable operation of the CHB, DC-link capacitors should have fixed and balanced voltage average values. In this paper, direct voltage error manipulation is used.

3) Harmonic reference current component: The SRF harmonic detection method is used here.

B. Grid Synchronization

PLL is the most commonly applied technique which is used here [2].

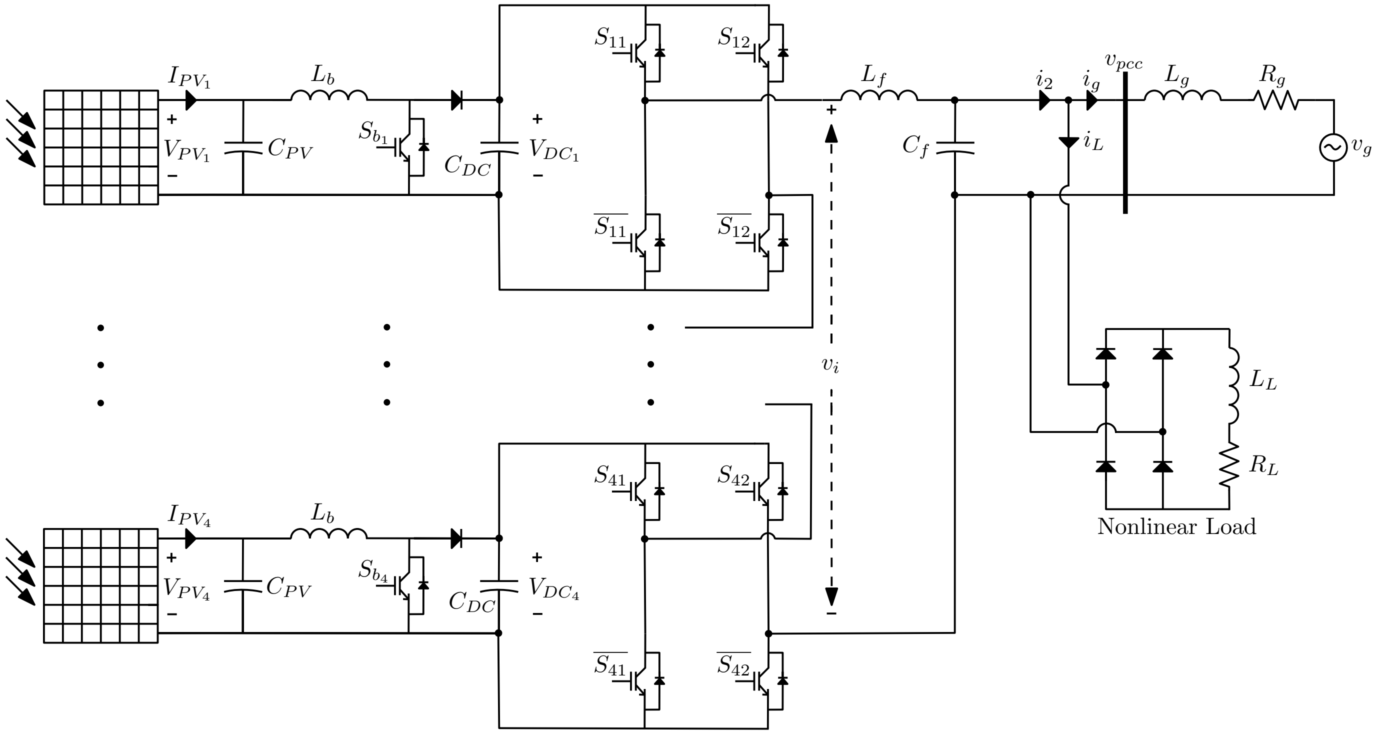

Fig. 1. Circuit diagram of the studied PV-fed CHB shunt APF.

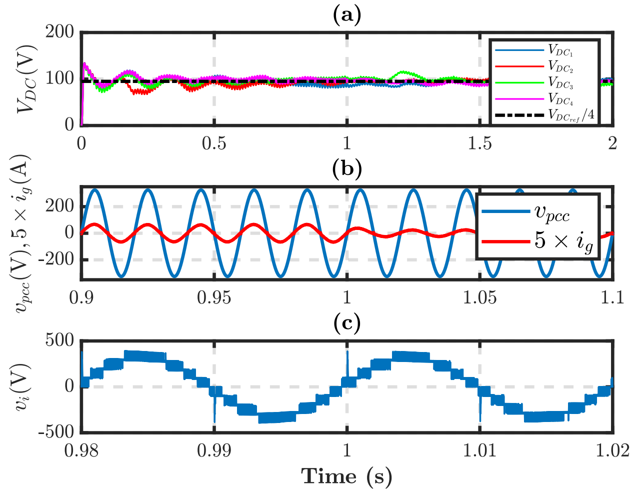

Fig. 2. The system performance under the same PV irradiation: (a) DC-link voltages of each CHB cell and their reference value; (b) Grid current and PCC voltage; (c) CHB inverter output voltage.

C. Current Control Loop

In the current control loop, as the reference signal is sinusoidal, a quasi-proportional resonant (quasi-PR) controller is employed [3].

D. CHB Modulation Method

In phase-shifted method, the same amplitude carriers are shifted π/H from each other for a H-cell CHB.

IV. SIMULATION RESULTS

To analyse the performance of the PV-fed CHB shunt APF, an irradiation step change for all PVs is applied at $t = 1$ s from $1000\,\mathrm{W/m^2}$ to $500\,\mathrm{W/m^2}$. Fig. 2(a) shows the system performance.

V. CONCLUSION

In this paper, a multi-functional grid-connected CHB inverter is studied. The system has the capability to extract the maximum available power from the PV sources and actively deliver it to the main grid with high power quality. Furthermore, the CHB inverter acting as a shunt APF can compensate harmonics and reactive power of the nonlinear local load. The whole control scheme including MPPT control of PV generators, shunt APF control, grid synchronization, and PWM control of switches is described in detail. The proposed system can also work with low switching frequency; hence, it can be practical in medium and high-voltage applications. The simulation results validate the system performance in severe operating conditions changes.

REFERENCES

[1] I. S. 519-2014, "IEEE recommended practice and requirements for harmonic control in electric power systems," *IEEE Std 519-2014 (Revision of IEEE Std 519-1992)*, pp. 1–29, 2014.

[2] Y. Hoon, M. A. Mohd Radzi, M. A. A. Mohd Zainuri, and M. A. M. Zawawi, "Shunt active power filter: A review on phase synchronization control techniques," *Electronics*, vol. 8, no. 7, 2019.

[3] N. Zhang, H. Tang, and C. Yao, "A systematic method for designing a PR controller and active damping of the LCL filter for single-phase grid-connected PV inverters," *Energies*, vol. 7, no. 6, pp. 3934–3954, 2014.

Gas Sensing Properties of Perovskite Decorated Graphene

Mohamed Ayoub Alouani, Juan Casanova Chafer, Xavier Vilanova

Universitat Rovira I Virgili
mohamedayoub.alouani@urv.cat, juan.casanova@urv.cat, xavier.vilanova@urv.cat

Abstract

This work explores the gas sensing properties of graphene nanolayers decorated with cubic Zinc Stannate (Zn_2SnO_4) nanoparticles (NPs) for the detection of toxic gases such as nitrogen dioxide (NO_2). The composition and structure of the synthesized nanoparticles and the nanocomposite were characterized using a wide variety of techniques such as X-Ray Diffraction, Field Emission Scanning Electron Microscopy and Transmission Electron Microscopy. High responses were obtained towards the NO_2 showing enhanced sensitivity when the graphene is decorated with Zn_2SnO_4 NPs in comparison to their bare graphene counterpart.

1. Introduction

Gas sensors play an increasingly important role in our modern society, particularly for monitoring the release of industrial pollutants and to preserve the public health security. The rapid detection of dangerous gases, such as nitrogen dioxide, is technologically essential as these atmospheric contamination is contributing to the greenhouse effect, and can be also dangerous for human health at low concentration levels. Chemoresistive sensors have been demonstrated as a promising technology for a real-time monitorization of these types of gases due to their high sensitivity, low cost, reproducibility and simplicity. Within the different nanomaterial available to develop active films, graphene stand out as an ideal candidate to develop chemoresistive devices owing to their high carrier density and mobility.

2. Materials and Methods

2.1. Zinc Stannate nanoparticles synthesis

Cubic Zinc Stannate nanoparticles were synthetized adapting the protocol proposed by Fakhrazad *et al*[1]. where ZnO and SnO_2 powders (99% purity) were mixed with molar ratio of ZnO:SnO2 (2:1). Then, the mixed powder was milled by hand for 30 min, and finally, the nanomaterial was annealed at 1000°C for 10 hours.

2.2. Graphene preparation and decoration

Graphene nanoplatelets from Strem Chemicals, Inc. (USA) were dispersed in 10 ml of a mixture of ethanol and methanol (80%-20% respectively) and then sonicated for 30 min. The same procedure was followed to disperse the synthesized Zn_2SnO_4 powders.

The decoration process consists of adding a specific volume of the Zn_2SnO_4 NPs solution in the graphene for obtaining a loadings of 5 and 20 %wt. Afterwards, the resulting solution was under constant stirring at 50°C for 30 min. Subsequently, the mixed solution was placed in a ultrasonication bath for 30 min.

2.3. Sensor Fabrication

The nanomaterials developed were deposited on commercial alumina sensors using a multiple droplet drop casting method at 70°C using a hot plate.

2.4. Material characterization

The synthesized nanoparticles and decorated graphene were characterized using different techniques such as the X-ray Diffraction (XRD), Raman and Field Emission Scanning Electron Microscopy (FESEM). Raman and XRD were used to prove the formation of the Zinc Stannate (Zn_2OSnO_4) phase and to study the crystal structure of the synthesized nanoparticles and finally, FESEM to check their dispersion on the graphene surface.

2.5. Gas Sensing Measurements

The resistance changes under NO_2 gas and experimental conditions were monitored using an Agilent HP 34972A multimeter connected a gas delivery system. The sensors were placed in an airtight sensing chamber.

3. Results

3.1 Material characterization

XRD graph presented in Figures 1 shows the formation of 93% of cubic phase zinc stannate with some traces of zinc oxide and tin oxide.

Besides, Raman spectroscopy was conducted to check the formation of the Zn_2OSnO_4 phase as shown in Figure 2. It can be observed two peaks corresponding to

---

[1] M Fakhrzad *et al* 2019 *Mater. Res. Express* **6** 095037

the target phase at 527 cm^{-1} and at 667 cm^{-1}.

Figure 3 shows an example of nanoparticle distribution through a FESEM image. The presence of the NP's as bright spots reveal a suitable dispersion over the graphene layer. A porous surface of the graphene was observed, which is also interesting from the gas sensing perspective.

3.2 Gas sensing Results

NO_2 detection was performed by applying repeated exposure and recovery cycles of increasing concentrations. Figure 4 shows the calibration curves obtained for 40-60-80-100 ppb of NO_2, in which graphene decorated with 20% of Zn_2SnO_4 Zinc Stannate NP's presents higher response (up to 2.5 times) compared to bare graphene at a considerably low temperature (50 ºC).

4. Conclusions

In summary, we have successfully synthesized cubic zinc stannate nanoparticles and used them for graphene decoration. As a result, a chemoresistive sensor with enhanced gas sensing properties was obtained. These decorated nanolayers have been showed promising results regarding NO_2 sensing at very low concentrations and at a relatively low temperature. It is also worth highlighting the slight enhancement effect of the different decoration percentages on the sensing performance. Specifically, the nanolayers containing a 20% of Zn_2SnO_4 shows better sensing responses to NO_2 than the 5% loading.

5. Graphs

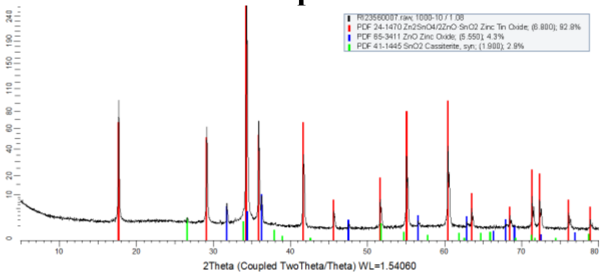

Figure 1. X-Ray Diffraction graph for the synthesized zinc stannate nanoparticles.

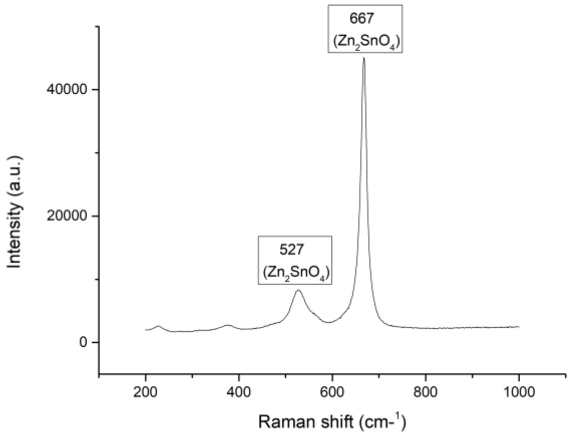

Figure 2 Raman spectrum of the formed Zn_2OSnO_4 phase.

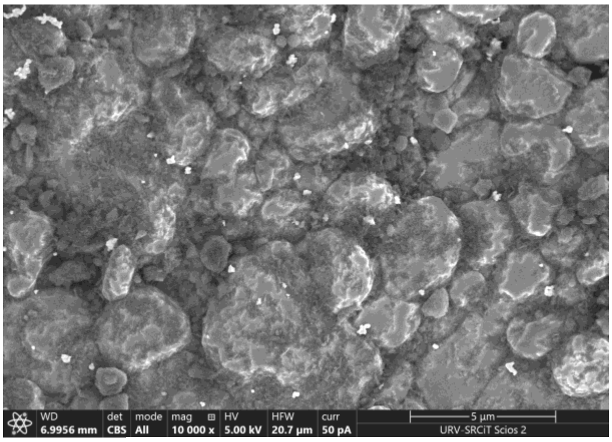

Figure 3. FESEM image recorded with Back-Scattered Electron (BSE) detector, showing the graphene decorated with 20% perovskite nanocrystals (bright spots).

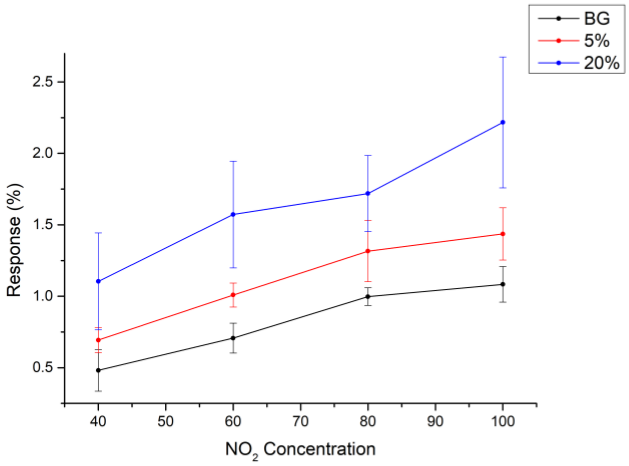

Figure 4. Calibration curves obtained for decorated bare Graphene (black), graphene loaded with 5 and 20% of zinc stannate NP (red and blue, respectively) when detecting different concentrations of NO_2 at ppb range.

A deep learning approach for identifying metabolites by mass spectrometry-based metabolomics

Muhammad Faizan Khan, Óscar Yanes Torrado & Roger Guimerà Manrique

Muhammadfaizan.khan@urv.cat

Abstract

We are building the first integrated methodology for non-targeted MS-based metabolomics, which involves annotating MS1 and MS2. The deep learning strategy will use variational autoencoders to represent MS/MS spectrum data and metabolite chemical structure. Integrated workflow will provide user-friendly apps to the scientific community.

MS/MS spectrum data and the chemical structure of known metabolites are represented using independent variational autoencoders. Encode the data with a convolutional neural network and decode with a Junction Tree Variational technique. ZINC was used to train JTVEA. Zinc is a drug database, not a metabolite database.

1. Introduction

For structural annotation, non-target metabolomics investigations depend on spectral libraries, yet current libraries are insufficient. Although in silico methods attempt to solve this problem, they are unable to discern between correct and incorrect annotations. As a result, assigning confidence to these annotations is the key challenge. According to the author, discovering and understanding novel metabolites is a costly, time-consuming, and labor-intensive process. The LC-MS technique can detect hundreds of thousands of molecules from a small sample. Individual molecules are fragmented and their masses are determined using tandem mass spectrometry (MS/MS). While public repositories of metabolomic LC-MS/MS data are rapidly rising, reusing these data at a repository scale remains challenging[1].

The identification of metabolites from mass spectrometry data requires annotation from MS1 and MS2 data, including reduction of redundant signals in MS1 (mostly due to in-source phenomena such as cation adduction) and matching observed MSn ($n \geq 2$) spectra to experimental spectra available in curated databases (e.g. HMDB, NIST) in MS2. However, a complication of this strategy is the poor coverage of primary and secondary metabolites (i.e., natural products) that may be detected from biological and environmental samples in terms of experimental spectra. For example, about 10% of known small molecules in compound-centric databases (e.g. METLIN and HMDB) have experimental spectral data from pure standards, although these databases currently contain >900,000 compounds (HMDB) and >110,000 compounds (METLIN). In addition, many metabolites are unknown so they are extremely difficult to characterize by the fact that both chemical structures of metabolites and annotated tandem MS spectra are unknown[2].

We are developing the first integrated workflow for non-targeted MS-based metabolomics, which includes annotating both MS1 and MS2. It will use the method described in patent (P202030061) for MS1 annotation, which will be coupled with a deep learning algorithm for MS2. The deep learning approach will use separate variational autoencoders to represent MS/MS spectral data and the chemical structure of known metabolites. User-friendly applications will be made available to the wider scientific community as a result of this integrated workflow[3].

2. Propose Methodology

A deep learning approach are develop to represent MS/MS spectrum data and the chemical structure of known metabolites using independent variational autoencoders. We encode the data using a convolutional neural network and decode using a Junction Tree Variational method. Regarding the dataset, JTVEA[4] was trained on the ZINC dataset. Zinc is not a metabolite database;it is a synthetic drug database. As a result, we use four metabolites datasets as training sets:NIST20, GNPS, HMDB, and MSDial.

3. Early Results

We used a metabolite dataset to train JTVAE, which had previously only been trained on drugs (ZINC). We come close to matching the ZINC dataset's results.

Figure 1 shows how much KL has been lost in each epoch. This shows that loss is higher in the early epochs, but it goes down after the sixth epoch.

Figure 2 shows Word accuracy over epoch. The accuracy of training and testing is clearly distinct. Overfitting is the term used to describe this type of behavior in deep Learning.

Figure 3 shows the topological accuracy over number of epochs.

Figure 4. shows the assemble accuracy over number of epochs.

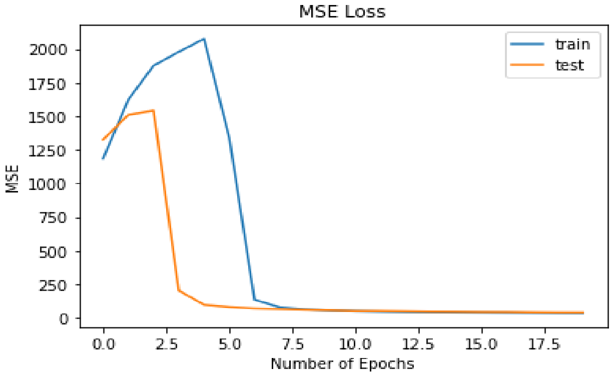

Figure 1 KL Loss

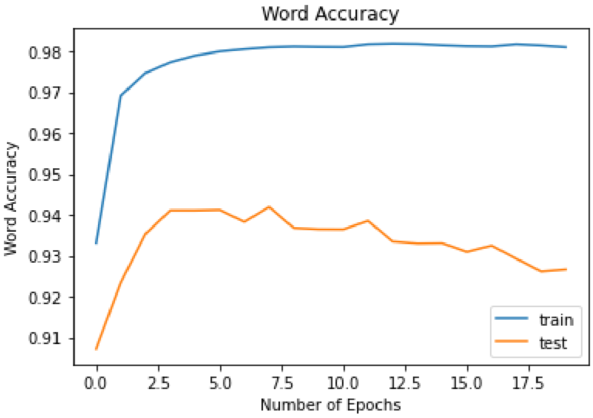

Figure 2 Word Accuracy

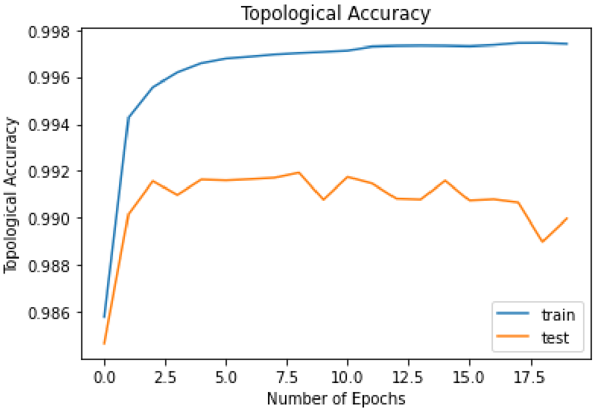

Figure 3 Topological Accuracy

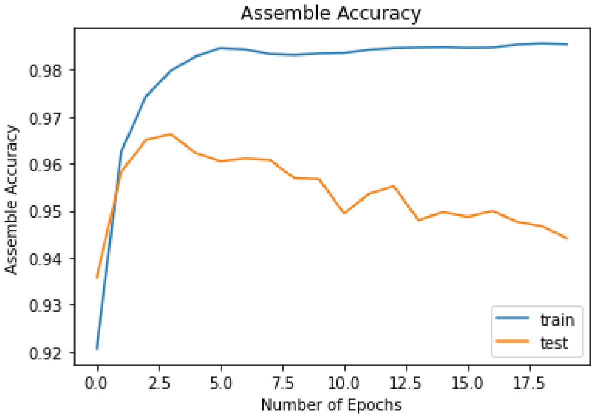

Figure 4 Assemble Accuracy

7. Conclusions

Here is three possible solutions to this problem:

1. Encode with JTVAE and decode with a basic CNN
2. Employ GCPN in conjunction with reinforcement learning
3. Representation of E.C. based on its sequence

This year and the following year, we will investigate all of these approaches in order to achieve our goal of predicting molecules from spectra.

References

[1] Choudhary, Kamal, et al. "Recent advances and applications of deep learning methods in materials science." *npj Computational Materials* 8.1 (2022): 1-26.
[2] Helin, Runar, et al. "On the possible benefits of deep learning for spectral preprocessing." *Journal of Chemometrics* 36.2 (2022): e3374.
[3] Wang, Yanbo, and Qianqian Song. "Disentangle VAE for Molecular Generation." *arXiv preprint arXiv:2202.06794* (2022).
[4] Jin, Wengong, Regina Barzilay, and Tommi Jaakkola. "Junction tree variational autoencoder for molecular graph generation." *International conference on machine learning*. PMLR, 2018.

Porous alumina based biosensing platform for early-stage infection diagnosis

Deepanshu Verma[1], Hedieh Haji Hashemi[1], Beatriz Prieto-Simón*[1,2]

[1]Department of Electronic Engineering, Universitat Rovira i Virgili, 43007 Tarragona, Spain
[2]ICREA, Pg. Lluís Companys 23, 08010, Barcelona, Spain
deepanshu.verma@urv.cat

Abstract

Ramifications that infections impose are consequential on global health. Infectious diseases significantly affect the healthcare systems resulting in an economic burden, especially on the developing countries.

Conventional *in vitro* diagnostics for infectious disorders take time and need centralized labs, knowledgeable staff, and heavy machinery. Recent developments in biosensor technology offer the potential to provide point-of-care diagnostics that are on par with or better than industry norms in terms of speed, accuracy, and price.

Herein, we present an electrochemical biosensing platform that is developed using porous anodic alumina membranes for the sensitive, rapid and label-free detection of exosomes as biomarkers for infectious disease diagnosis.

1. Introduction

Given the huge number of projected fatalities, the risks of pandemics and epidemics, and the antibiotic resistance of many pathogens, biosensors are frequently employed in healthcare, notably for the identification of infectious diseases[1].

The overuse of antibiotics, the spread of bacteria that are multidrug resistant (MDR), the advent of novel infectious agents, and the ease with which illnesses can spread quickly owing to population growth and globalization are the main obstacles to the treatment of infectious diseases. Successful clinical management of infectious illnesses depends on prompt diagnosis [2].

Currently, a variety of laboratory-based tests, such as those based on microscopy, cell culture, immunoassays, and nucleic-acid amplification, are used to diagnose clinically significant infectious diseases carried on by bacteria (such as pneumonia), mycobacteria (such as tuberculosis), viruses (such as HIV, hepatitis), fungi (such as candidiasis), and parasites (such as malaria). Despite being predominantly utilized methods, they have well-known drawbacks. For instance, in many clinical situations, microscopy lacks sensitivity, and cell culture takes a very long period. While molecular specificity is offered by nucleic-acid amplification techniques like PCR, they require extensive sample preparation and carry the risk of false positive results[3].

Over the recent past, the focus has shifted towards the development of comprehensive methods to identify biomarkers for the detection of infectious diseases and the quest for highly sensitive and specific biomarkers have presented new opportunities[4].

Exosomes are one such biomarker of interest. They are extracellular vesicles with a diameter typically in the range of 30 nm – 150 nm. Exosomes have been increasingly studied for their role in direct cell-cell communication for both biological and pathological processes[5]. They are known to carry genetic load with a capability of delivering information vital for cell survival.

Capture and detection of exosomal content (RNA, protein, lipids etc.) can provide quantitative information for early-stage detection. Infected cells communicate with each other through exosome-like vesicles to promote features such as population density. Diagnostic tools with the capability to capture these identified exosomes could help better the treatment decisions or on-site analysis.

Conventionally, exosome isolation is tedious, involves experimental variability and requires trained personnel. The best method in practice to isolate and purify exosomes from biological fluids is ultracentrifugation. Multiple ultracentrifugation steps are performed, followed by density gradient ultracentrifugation to isolate exosomes from co-purified proteins and other membranous vesicles.

Therefore, it is crucial to design a reliable biosensor to detect exosomes enabling the diagnosis of infections at their onset. A label-free electrochemical platform featuring aligned nanochannels of porous alumina is presented. The focus is to develop a low-cost point-of-care testing tool for exosome capture and quantification.

Porous anodic alumina provides outstanding features as a biosensing platform. The use of porous alumina offers an advantage over conventional sensing platforms because of their intrinsic property of forming self-ordered, uniform and homogenous nanochannels. This also provides the porous alumina an edge over the other porous nanostructures because they offer enhanced reproducibility leading to higher accuracy.

The electrochemical detection is based on the principle of pore blockage owing to the capture of exosomes by the immobilized bioreceptor (e.g. antibodies) within the nanochannels (Figure 1). The exosome-antibody complex restricts the diffusion of redox species towards the carbon working electrode, which is placed below the modified porous alumina membrane enclosed in a custom-built Teflon cell with external reference and counter electrodes.

Electrochemical impedance spectroscopy (EIS) and square-wave voltammetry (SWV) are used as analytical techniques for sensing. In response to the partial blockage occurring in the nanochannels, EIS monitors the changes that happen on the electrode surface, as upon binding of a new layer on the membrane, the diffusion of the redox species through the nanochannels is hindered and thus capacitance and charge transfer resistance of the electrode change. Similarly, in SWV, a decrease in the oxidation current of the redox species occurs at the electrode surface. These are used as analytical responses by the biosensors to quantitatively recognize the capture of a target analyte.

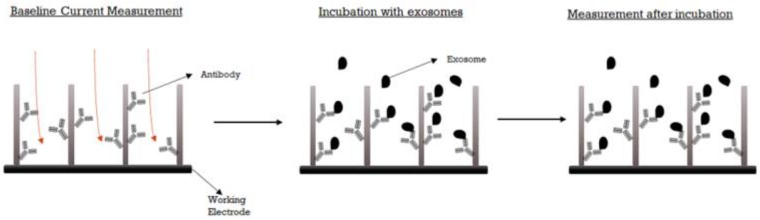

Figure 1: Schematic representation of NAA electrochemical sensing based on pore blockage

References

1. S. Sahoo, S. N. Sahu, S. kumar Pattanayak, N. Misra, and M. Suar, Biosensor and its implementation in diagnosis of infectious diseases. Elsevier Inc., 2020.
2. D. Mabey, R. W. Peeling, A. Ustianowski, and M. D. Perkins, “Diagnostics for the developing world,” Nat. Rev. Microbiol., vol. 2, no. 3, pp. 231–240, 2004, doi: 10.1038/nrmicro841.
3. S. M.L., M. K.E., W. P.K., and L. J.C., “Advances and challenges in biosensor-based diagnosis of infectious diseases,” Expert Rev. Mol. Diagn., vol. 14, pp. 225–244, 2014, [Online]. Available:
4. Hwang H, Hwang BY, Bueno J. Biomarkers in Infectious Diseases. *Dis Markers*. 2018;2018:8509127. Published 2018 Jun 20. doi:10.1155/2018/8509127
5. Hanjani NA, Esmaelizad N, Zanganeh S, Gharavi AT, Heidarizadeh P, Radfar M, Omidi F, MacLoughlin R, Doroudian M. Emerging role of exosomes as biomarkers in cancer treatment and diagnosis. Crit Rev Oncol Hematol. 2022 Jan;169:103565. doi: 10.1016/j.critrevonc.2021.103565. Epub 2021 Dec 3. PMID: 34871719.

Novel Carbazole-Based Conjugated Molecules as Self-Assembled Hole Transporting Monolayers for Inverted Perovskite Solar Cells

Dora A. González*[1,2], **Carlos E. Puerto Galvis**[1], **Ece Aktas**[1,3], **Eugenia Martínez-Ferrero**[1], **Emilio Palomares**[1,4]

[1] *Institute of Chemical Research of Catalonia (ICIQ-BIST), Avda. Països Catalans, 16, 43007 Tarragona, Spain*

** E-mail: dagonzalez@iciq.es*

[2] *Departamant d'Enginyeria Electrònica, Eèctrica i Automàtica. URV. Tarragona, 43007. Spain*

[3] *Current address: Department of Chemical, Materials and Production Engineering, University of Naples Federico II, Piazzale Tecchio 80, 80125 Fuorigrotta, Italy*

[4] *Catalan Institution for Research and Advanced Studies (ICREA), 08010 Barcelona, Spain*

Abstract

Renewable solar energy is considered the main candidate to provide clean and green energy for the upcoming years. Among the different types of photovoltaic technologies available, inverted perovskite solar cells (IPSCs) is a promising approach due to their easy fabrication and low manufacturing cost with minimum environmental impact.[1] Inverted structure (p-i-n configuration) consists basically in a light-absorbing perovskite layer which is sandwiched between a hole transport material (HTM) and an electron transport material (ETM) (**Fig 1a**).[2]

The use of organic self-assembled monolayers (SAMs), as HTM in the interface of IPSC devices, has recently attracted attention because of their easy preparation, low costs, good solution deposition and the ability to tune the properties of these materials by modifying their chemical structure[3]. In this work, we report the synthesis of a carbazole-based novel SAMs for IPSCs.

1. Introduction

One of the main topics of research in the IPSCs field has been the replacement of the wide used Poly(triaryl amine) (PTAA) is the most used HTM for IPSCs, reaching efficiencies up to 23.7%[4] However, its production cost, and unstable in devices that point out the need of designing and synthesizing new HTM for inverted structure.

Thus, in the las few years, a variety of SAMs have been synthesized, in order to find easily synthetic routes and more stable molecules.[1]

SAMs based on the carbazole moiety have received much attention due to their chemical structure with versatile and advantageous characteristics such as the low cost of the starting material (9H-carbazole), good chemical stability, easy functionalization and high solubility in common solvents among others.[1,5]

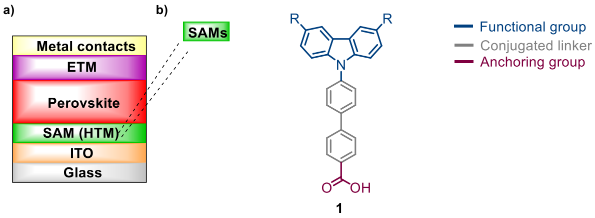

Figure 1. a) Inverted perovskite solar cell device architecture, b) chemical structure and constituents of SAMs synthesized in this study.

2. HTM-SAMs

The chemical structure of the SAM for IPSCs is extracting holes created in the perovskite when it absorbs light and transporting them towards the corresponding electrode.[6] In order to improve the charge extraction, the principal characteristics that have to present a good SAM are: high solubility in common solvents, photochemical stability and energy levels that fit with perovskite's.[2,7]

This work aims to design and synthesize new carbazole-based conjugated molecules, featuring special functional groups, to study and understand the effects and interactions at the SAM/perovskite interface.

Thus, setting the carboxylic acid function (-COOH) as an anchoring group and the biphenyl moiety as a conjugated spacer linker, different functional groups, were included in the carbazole core of the prepared

SAMs **(Fig. 1b)** to study and understand the effects and interactions at the SAM/perovskite interface, which finally allow us to obtain IPSCs with high performance.

3. Results and conclusions

The reactions involved in the synthesis of the new SAMs **(DREA-03 and DREA-04)** consisted first of Carbazole-DA synthesized according to literature procedures[8]. After that, the coupling of the unit using Buchwald-Hartwig amination was carried out using $Pd_2(dba)_3$ as a catalyst. Finally, reduction to carboxylic acid to obtain the desired product **DREA-03 and DREA-04 (Scheme 1)**.

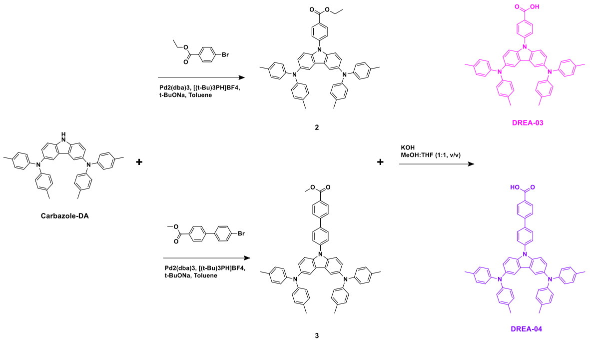

Scheme 1. The synthetic routes of DREA-03 and DREA-04.

All the new compounds were well characterized by spectroscopy and spectrometric techniques.

However, the inverted structure (p-i-n) in perovskite solar cell has been used to study and select a commercial HTM (PTAA) for use as a reference. Where PTAA was studied with different methods. After studying the PTAA, emphasis will be placed on the IPSC optimization to improve the development of bottom contact layer strategies to understand the interface between HTL/perovskite for further improvement of the performance of those devices.

The following table shows the best cell parameters we got was with PTAA. Which will be used as a reference to compare it with our synthesized SAMs for its better performance.

Table 1. The best cell parameters of the devices fabricated PTAA derived from J-V curves (Figure 2)

HTM		Jsc (mA/cm^2)	Voc (V)	FF (%)	PCE (%)
PTAA	forward	22.23	1.109	75.2	18.53
	reverse	22.21	1.11	74.8	18.44

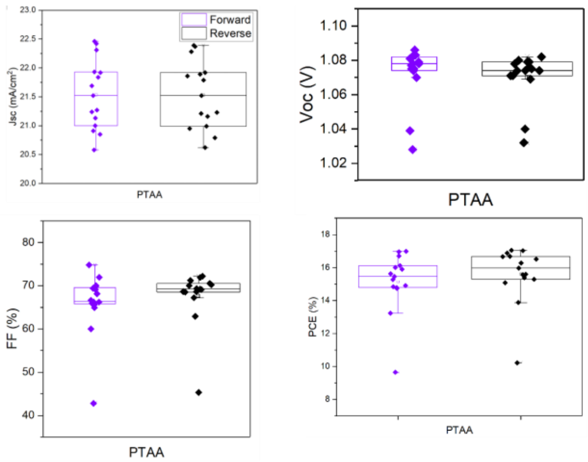

Figure 2: Photovoltaic parameters of the best performing devices with the different HTL deposited by spin-coating

4. References

1. Ali, F., Roldán-Carmona, C., Sohail, M. & Nazeeruddin, M. K. Applications of Self-Assembled Monolayers for Perovskite Solar Cells Interface Engineering to Address Efficiency and Stability. *Advanced Energy Materials* vol. 10 (2020).
2. Yalcin, E. *et al.* Semiconductor self-assembled monolayers as selective contacts for efficient PiN perovskite solar cells. *Energy Environ. Sci.* **12**, 230–237 (2019).
3. Aktas, E. *et al.* Understanding the perovskite/self-assembled selective contact interface for ultra-stable and highly efficient p-i-n perovskite solar cells. *Energy Environ. Sci.* **14**, 3976–3985 (2021).
4. Degani, M. *et al.* 23.7% Efficient inverted perovskite solar cells by dual interfacial modification. *Sci. Adv.* **7**, 1–10 (2021).
5. Al-Ashouri, A. *et al.* Conformal monolayer contacts with lossless interfaces for perovskite single junction and monolithic tandem solar cells. *Energy Environ. Sci.* **12**, 3356–3369 (2019).
6. Schreiber, F. Structure and growth of self-assembling monolayers. *Prog. Surf. Sci.* **65**, 151–257 (2000).
7. Gooding, J. J., Mearns, F., Yang, W. & Liu, J. Self-assembled monolayers into the 21st century: Recent advances and applications. *Electroanalysis* **15**, 81–96 (2003).
8. Xu, B. *et al.* Carbazole-Based Hole-Transport Materials for Efficient Solid-State Dye-Sensitized Solar Cells and Perovskite Solar Cells. *Adv. Mater.* **26**, 6629–6634 (2014).

Cleaning Mass Spectrometry Imaging data using a matrix perspective

Lluc Sementé[1], Gerard Baquer[1], Toufik Mahamdi[1], Xavier Correig[1,2,3], María García-Altares[1,2], Pere Ràfols[1,2,3]

[1] University Rovira I Virgili, Department of Electronic Engineering, Tarragona, Spain.
[2] Spanish Biomedical Research Center in Diabetes and Associated Metabolic Disorders (CIBERDEM), 28029, Madrid, Spain.
[3] Institut D'Investigacio Sanitaria Pere Virgili, Tarragona, Spain.

Abstract

Mass spectrometry imaging provides multidimensional datasets of mass-to-charge (*m/z*) images usually analyzed by comparing molecular signatures from different regions. To facilitate this task, we developed rMSIKeyIon, a software package that compares regions in a tissue sample automatically. From the development of the tool we detected two major drawbacks in our workflow.

First, we notice that multiple m/z images shared the same chemical information by studying their spatial distributions. This was produced mostly by isotopic ions crowding our datasets. Second, we observed that some pixels were not representative of the region assigned to them, as they were not well correlated with any of the spatial regions under use. To explain this we assumed the idea of transition regions; tissue regions where different types of tissue were mixed.

To face the first drawback we developed rMSIannotation, a peak annotation tool which automatically detects isotopic and adduct ions using a novel library-free criterion. The criterion developed is based on integrating a model of libraries of compounds in the tool instead of consulting libraries in runtime, which result in faster executions. The results show that rMSIannotation is capable of detecting most of the isotopic patterns in mass spectra, both from high and ultra-high mass resolution datasets.

To face the second problem we investigated the notion of soft clustering by applying the Fuzzy c-means algorithm in MSI datasets. Soft clustering assigns multiple clusters to the same pixel and allows to qualify each of them with a membership degree. This is useful for identifying transition regions, and for comparing the molecular signature of only the pixels with high degree of membership to a particular region.

1. Introduction

Mass Spectrometry Imaging produces big (multiple gigas to teras) multidimensional data structures explaining the molecular composition of a tissue section.[1] The data is organized in a group of molecular images representing the intensity distribution of all the ions with a particular mass-to-charge (*m/z*) at each pixel of the image. The multidimensional data structure can be represented as a matrix in which, the columns are all the *m/z* values registered by the instrument and the rows refer to each of the sample points (pixels in the image). Using this matrix perspective it is possible to obtain the mass spectrum of a sample point by reading a row or obtaining an image by visualizing the spatial distribution of a column using the pixel coordinates.[2] But, the raw data contains a lot of useless data in the form of *m/z* values without intensity or pixels without spectrum, enlarging the dataset unnecessarily and slowing down the analysis of the data. To solve it, multiple data processing strategies are used including, spectrum smoothing, spectrum alignment, mass calibration, peak detection, and peak binning, which result in a reduced matrix.[3]

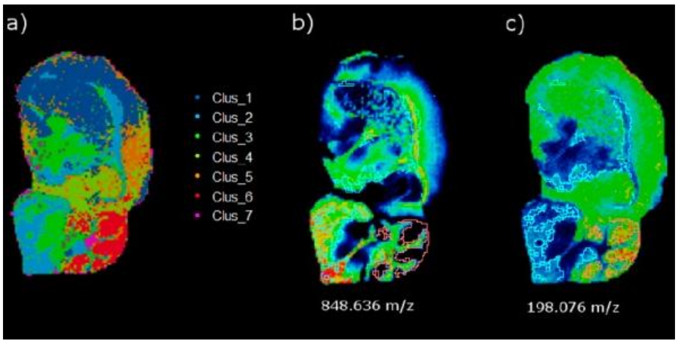

Fig.1. a) Clustering of a mouse brain slide. **b)** Intensity distribution of ion *m/z* 848.636 which is up-regulated in cluster 2 compared to cluster 6. **c)** Intensity distribution of ion *m/z* 198.076 which is down-regulated in cluster 2 compared to cluster 6.

A common approach to the analysis of these data structures is comparing the *m/z* signature of different groups of pixels, this is, comparing the molecular composition of different tissue regions. To automatize this task we developed rMSIKeyIon[4], an R package capable of comparing pair-wise all the previously defined regions in a MSI dataset. The tool compares the intensity distribution of the *m/z* peaks using the fold change, the Mann-Whitney U statistic, and the percentage of pixels in which the peak is not detected in the region. Figure 1 shows a clustering of a mouse brain and two ions detected by rMSIKeyIon that are up-regulated and down-regulated in cluster 2 compared to cluster 6. From the results of rMSIKeyIon we detected two important features to improve separated between the *m/z* peaks perspective and in the pixel perspective. The first, being the presence of columns with redundant information due to the presence of isotopes, and the second being the presence of rows with pixels with characteristics from multiple clusters associated with only one cluster.

2. Column perspective: isotopic ions

To deal with the redundant column problem we developed a peak annotation tool. Peak annotation is the procedure of giving a chemical identity of certain degree to the *m/z* peaks in a mass spectrometry dataset. This information can consist of discerning if a *m/z* peak is an isotope of another *m/z* peak or a different adduct of the same molecule, a molecular formula or even a molecular structure. For our goal we were interested in the first part, detecting isotopes and adducts, as it helps in reducing the number of columns and additionally, with MSI is not possible to go further than a putative molecular formula assignation, as MSI does not produce molecular structure information.

We developed rMSIannotation[5], a MSI peak annotation tool that annotates carbon-based isotopes and adducts without using external libraries of compounds, which allows shorter runtimes compared to other approaches. This is achieved by using a novel criterion consisting of the inclusion in the tool of a model of the isotopic intensity rations of metabolites over the *m/z* axis. The model was build using the Human Metabolome Database (HMDB)[6] and a simple linear regression. We tested our approach with MSI datasets manually annotated using additional analytical techniques and compared it with the peak annotation tool METASPACE[7] available for MSI, which is based in consulting libraries in runtime. rMSIannotation performed better in replicating the manually annotated peaks than METASCPAE. Additionally, with our model we were able to find specific algae metabolites outside the HMDB in an ultra-high resolution algae dataset[8], proving that the model approach can find results outside of the modeled libraries.

3. Row perspective: transition pixels

To face the problem of pixels related to multiple clusters we introduced the notion of soft clustering in our workflow, particularly the fuzzy c-means algorithm[9] which had some traceback of use in MSI[10]. Fuzzy c-means assigns to each pixel a membership value to each of the clusters and the sum of all the membership values of a pixels is one. The pixels with high memberships values for just one cluster are the pixels that represent the molecular signature of the tissue region in that cluster. To assess which pixels fall into this category we developed the pixel fidelity score (PFS), which is a measure between 0 and 1 that combines all the membership values of a pixel and retrieves values close to 1 for pixels with exclusivity for one cluster.

Thresholding the PFS we were able to compare the differences in molecular signatures between regions excluding the pixels that are not representative of just one cluster and compared it with removing randomly the number of pixels. Figure 2 shows an increase in fold change values and a lesser reduction of significance of the PFS thresholding method compared to the random sampling. Additionally, using the PFS we were able to find structures in a mouse cerebellum that the clustering algorithm could not group together. This shows that using soft clustering there is more change of evaluating the results obtained compared to hard clustering thanks the pixel membership to cluster.

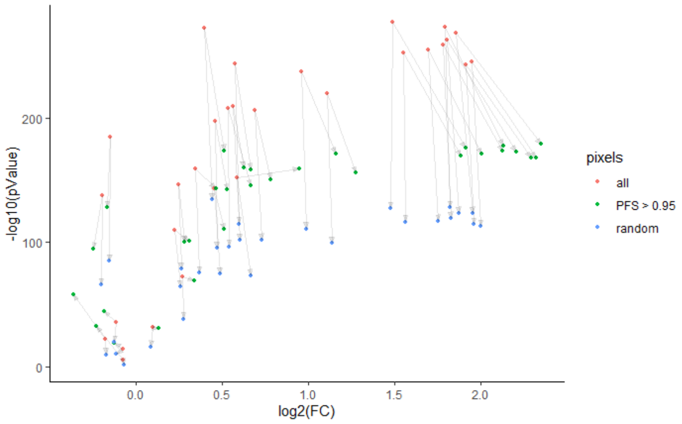

Fig.2. a) Differences between pixel removing procedures. The color scale indicates which pixels were removed before comparing clusters. The total number of pixels removed in both procedures is the same. The arrows indicate how the fold change and the significance of an *m/z* feature change after removing pixels using each method.

Finally, we developed a workflow for MSI to analyze the presence of cancer tissue in a human head and neck cancer dataset using soft clustering. With Fuzzy c-means and PFS we were able to observe the differences in membership between the cluster associated with cancer and the cluster associated with normal tissue in tissue slides that were classified as transition between both tissues. Figure 3 summaries the findings of the workflow.

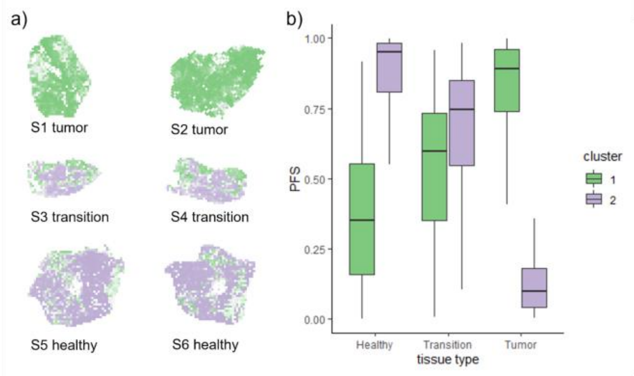

Fig.3. a) Clustering result of all the tissues in the head and neck dataset using two clusters and using the transparency as membership scale. **b)** PFS distribution per cluster and per tissue type of the clustering results of all the samples.

7. Conclusions

The two strategies presented deal with problems that arise from the two perspectives of looking into the MSI dataset: the pixels and the *m/z* peaks. Both strategies not only are useful for removing data, which benefits are faster execution times and reduction of redundancy, but they also increase the information of the remaining elements by introducing and identity label in the form of isotope or adduct for the *m/z* peaks, and a degree of membership to the cluster for the pixel.

References

[1] T. C. Rohner, D. Staab, and M. Stoeckli, “MALDI mass spectrometric imaging of biological tissue sections,” *Mech. Ageing Dev.*, vol. 126, no. 1, pp. 177–185, 2005.

[2] P. Ràfols *et al.*, “rMSIproc: an R package for mass spectrometry imaging data processing,” *Bioinformatics*, vol. 36, no. 11, pp. 3618–3619, 2020.

[3] P. Ràfols *et al.*, “Signal preprocessing, multivariate analysis and software tools for MA(LDI)-TOF mass spectrometry imaging for biological applications,” *Mass Spectrom. Rev.*, vol. 37, no. 3, pp. 281–306, May 2018.

[4] E. Del Castillo *et al.*, “RMsikeyion: An ion filtering r package for untargeted analysis of metabolomic LDI-MS images,” *Metabolites*, vol. 9, no. 8, 2019.

[5] L. Sementé, G. Baquer, M. García-Altares, X. Correig-Blanchar, and P. Ràfols, “rMSIannotation: a peak annotation tool for mass spectrometry imaging based on the analysis of isotopic intensity ratios,” *Anal. Chim. Acta*, vol. 1171, p. 338669, 2021.

[6] D. S. Wishart *et al.*, “HMDB 4.0: The human metabolome database for 2018,” *Nucleic Acids Res.*, 2018.

[7] A. Palmer *et al.*, “FDR-controlled metabolite annotation for high-resolution imaging mass spectrometry,” *Nat. Methods*, vol. 14, no. 1, pp. 57–60, Jan. 2017.

[8] G. Schleyer *et al.*, “In plaque-mass spectrometry imaging of a bloom-forming alga during viral infection reveals a metabolic shift towards odd-chain fatty acid lipids,” *Nat. Microbiol.*, vol. 4, no. 3, pp. 527–538, 2019.

[9] D. Graves and W. Pedrycz, “Fuzzy C-Means, Gustafson-Kessel FCM, and Kernel-Based FCM: A Comparative Study,” pp. 140–149, 2007.

[10] S. Sarkari, C. D. Kaddi, R. V. Bennett, F. M. Fernandez, and M. D. Wang, “Comparison of clustering pipelines for the analysis of mass spectrometry imaging data,” *2014 36th Annu. Int. Conf. IEEE Eng. Med. Biol. Soc. EMBC 2014*, pp. 4771–4774, 2014.